Cell

Super-Resolution Imaging of the Extracellular Space in Living Brain Tissue

Graphical Abstract

Highlights

- 3D-STED and labeling of extracellular fluid for nanoscale imaging of live brain ECS

- As negative imprint of all cells, it captures anatomical complexity of brain tissue

- Activity-induced ECS remodeling and cell migration in visible neuropil is revealed

- Super-resolution imaging paradigm immune to bleaching and with reduced toxicity
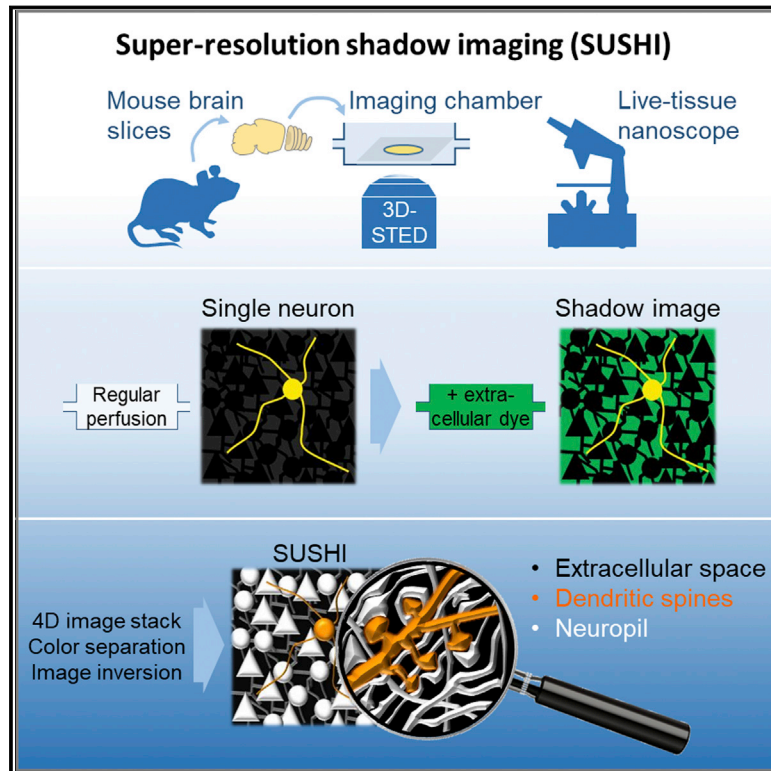
Authors

Jan Tønnesen, V.V.G. Krishna Inavalli, U. Valentin Nägerl

Correspondence

valentin.nagerl@u-bordeaux.fr

In Brief

Live tissue super-resolution 3D-STED microscopy combined with fluorescence labeling of the interstitial fluid reveals the complex spatial organization of the extracellular space of the brain.

CellPress

Super-Resolution Imaging of the Extracellular Space in Living Brain Tissue

Jan Tønnesen,[1,2,3,4] V.V.G. Krishna Inavalli,[1,2] and U. Valentin Nägerl[1,2,5,*]

[1]University of Bordeaux, 33077 Bordeaux, France
[2]Interdisciplinary Institute for Neuroscience, CNRS UMR 5297, 33077 Bordeaux, France
[3]Department of Neuroscience, University of the Basque Country UPV/EHU, 48940 Leioa, Spain
[4]Achucarro Basque Center for Neuroscience, 48940 Leioa, Spain
[5]Lead Contact
*Correspondence: valentin.nagerl@u-bordeaux.fr
 https://doi.org/10.1016/j.cell.2018.02.007

SUMMARY

The extracellular space (ECS) of the brain has an extremely complex spatial organization, which has defied conventional light microscopy. Consequently, despite a marked interest in the physiological roles of brain ECS, its structure and dynamics remain largely inaccessible for experimenters. We combined 3D-STED microscopy and fluorescent labeling of the extracellular fluid to develop super-resolution shadow imaging (SUSHI) of brain ECS in living organotypic brain slices. SUSHI enables quantitative analysis of ECS structure and reveals dynamics on multiple scales in response to a variety of physiological stimuli. Because SUSHI produces sharp negative images of all cellular structures, it also enables unbiased imaging of unlabeled brain cells with respect to their anatomical context. Moreover, the extracellular labeling strategy greatly alleviates problems of photobleaching and phototoxicity associated with traditional imaging approaches. As a straightforward variant of STED microscopy, SUSHI provides unprecedented access to the structure and dynamics of live brain ECS and neuropil.

INTRODUCTION

All brain cells are surrounded by a narrow extracellular space (ECS), which is filled with extracellular fluid and molecules of the extracellular matrix. The ECS has a reticular structure that forms a reservoir for ions and corridor for nutrients from the blood stream. It is critical for brain homeostasis and metabolite clearance and serves as a channel for extrasynaptic signaling by volume transmission (Lei et al., 2017; Nicholson and Hrabětová, 2017; Syková and Nicholson, 2008).

Large changes in brain ECS volume fraction and metabolite clearance during the sleep-wake cycle in mouse cortex have recently been reported (Ding et al., 2016; Xie et al., 2013), suggesting that the ECS plays an active regulatory role in brain physiology. Yet, very little is known about the spatial orga-

nization and dynamics of the ECS, owing primarily to a lack of appropriate techniques.

As a negative imprint of the cells that make up brain tissue, the ECS can be thought of as a convoluted network of connected sheets and tubes, whose dimensions extend well below the diffraction barrier of conventional optical microscopy (Thorne and Nicholson, 2006). Accordingly, the ECS and the neuropil of interwoven neural structures look like an amorphous mass in conventional light microscopy, including confocal or 2-photon microscopy.

Our current view of brain ECS derives almost exclusively from electron microscopy (EM) of chemically fixed tissue, where it appears as a uniformly thin layer (Harris and Stevens, 1989). However, EM studies based on cryo-fixation have suggested a much more heterogeneous and voluminous organization (Korogod et al., 2015; Vanharreveld et al., 1965). This is supported by biophysical measurements, which indicate that the ECS takes up 15%–30% of total brain volume (Lehmenkühler et al., 1993; Syková and Nicholson, 2008; Van Harreveld and Steiner, 1970).

Whereas EM is incompatible with live tissue imaging, super-resolution microscopy has the potential to break new ground in studying brain ECS. Single-molecule tracking of carbon nanotubes was recently used to explore the diffusional properties of the ECS and provided first glimpses of its morphology in living brain slices (Godin et al., 2017). Stimulated emission depletion (STED) microscopy is a volumetric super-resolution imaging technique that has been successfully used for analyzing nanoscale neural morphology in live tissue (Berning et al., 2012; Chéreau et al., 2017; Panatier et al., 2014; Tønnesen et al., 2014) and thus is potentially well suited to image ECS structure.

In the standard STED approach, fluorescence is quenched in a doughnut-shaped area around the excitation spot, which improves spatial resolution selectively in the x-y plane. However, spatial resolution can be simultaneously enhanced in the z direction by distributing the STED light intensity more isotropically around the excitation focus (3D-STED) (Lenz et al., 2014; Wildanger et al., 2009).

Since STED microscopy relies on a de-excitation laser beam in addition to the excitation laser beam, it involves more photons and is more prone to photobleaching and toxicity than regular fluorescence microscopy. While the problem of photobleaching can be mitigated by volumetric imaging of diffusible fluorescent markers (Nägerl et al., 2008; Urban et al., 2011) and by

sophisticated technological solutions (Danzl et al., 2016), phototoxicity still imposes severe restrictions on time-lapse imaging.

To visualize the spatial organization of the ECS in live brain tissue, we developed super-resolution shadow imaging (SUSHI). It is based on 3D-STED microscopy and labeling of the extracellular fluid with a diffusible fluorophore that does not permeate cell membranes. The extracellular labeling scheme is effectively insensitive to photobleaching and permits intense 3D-STED time-lapse imaging of large fields of view without signs of phototoxicity.

Using mouse organotypic hippocampal slices, we show that SUSHI gives unprecedented optical access to the structure and dynamics of the ECS. We document distinctive ECS structural changes in response to a variety of physiologically relevant stimuli, including osmotic challenges, epileptiform discharges and glutamate uncaging.

Moreover, as SUSHI produces super-resolved negative images of all cells, it reveals the micro-anatomical organization of live brain tissue in its entirety. This makes it possible to detect synaptic clefts, to generate 3D reconstructions of unlabeled cells, to visualize perineuronal spaces, and to monitor cell migration while the surrounding anatomical context is also visible.

RESULTS

Spatial Resolution of 3D-STED

We constructed a STED microscope based on pulsed lasers for fluorescence excitation ($\lambda = 485$ nm) and STED quenching ($\lambda = 597$ nm), which was equipped with a heated perfusion chamber to image living organotypic brain slices through an inverted objective (Figure 1A, left). A combination of helical and annular delay phase masks was used to shape the point-spread function (PSF) of the STED beam in 3D (Figure 1A, right). Using an oil objective with a numerical aperture of 1.47, it yielded a spatial resolution of around 60 nm in x-y and 160 nm in z, based on imaging 40 nm fluorescent beads on glass coverslips (Figure 1B), which corresponds to a volume resolution of under 1 attoliter (<0.001 μm^3). A glycerol objective gave a slightly larger PSF (Figure S1), as expected given its lower numerical aperture of 1.3; however, it had a correction collar to reduce spherical aberrations (Figure S1), which otherwise degrade the PSF when imaging deeper in the tissue (Urban et al., 2011). For comparison, the typical volume resolution of a commercial 2-photon microscope with a standard 1.0 NA (numerical aperture) objective is around a quarter femtoliter (>0.25 μm^3) and thus can only poorly resolve structures on this spatial scale (Figure 1C).

SUSHI of Live Brain ECS

Given the high spatial resolution of our 3D-STED approach, we reasoned it might be possible to visualize directly the ECS by perfusing brain slices with fluorescently labeled artificial cerebrospinal fluid (ACSF), provided the dye molecules penetrate well into the ECS but remain outside of cells.

Indeed, using standard cell biology fluorescent dyes, such as calcein and Alexa Fluor 488, the labeling strategy enabled visualization of the ECS and simultaneously projected cell bodies and their processes as dark voids resembling shadows in the surrounding fluorescence (Figure 1D). To facilitate visual perception of structure and contrast in the image, we inverted the grayscale

lookup table so that the interstitial spaces appear dark and cellular structures bright (Figure 1E and all subsequent images). The ECS appeared highly heterogeneous: dense and compact in some places but slack and voluminous in others, frequently featuring larger reservoirs next to cell bodies (Figures 1E, S2, and S3A).

SUSHI can produce crisp images down to 50 μm tissue depth when using the glycerol objective (Figure S3B) and proves to be a simple strategy to visualize unlabeled, living dissociated neurons (Figure S3C). Moreover, the dye can be delivered by local injection via a patch-pipette, demonstrating the ease and versatility of the extracellular labeling strategy (Figure S3D).

We compared image quality between 2-photon and 3D-STED microscopy. While structural details were filtered out by the larger 2-photon PSF and disappeared in the 2-photon images (Figure S3E), the 3D-STED approach produced sharp and detail-rich images of the ECS and thereby also clearly delineated axons and dendrites of the neuropil (Figure S3F). Consistently, line intensity profiles through the ECS revealed higher spatial variation in STED than in 2-photon images, owing to the gain in volume resolution (Figures S3E–S3I).

To find out whether the molecular size of the dye influences how it spreads in the ECS, we co-perfused slices with two spectrally distinguishable dyes of very different molecular weights (Atto-514: 0.86 kDa and Alexa Fluor 488-dextran: 10 kDa). The merged fluorescence signals overlaid well everywhere (Figure S3J), indicating that the dyes were not differentially distributed in the ECS, including the voluminous perineuronal spaces.

Extracellular Dye Loading

To assess the suitability of SUSHI for neurophysiological studies, we characterized the ECS labeling method with respect to cellular uptake, tissue wash-out, photobleaching, and potentially adverse effects on neuronal function.

Within minutes of perfusing the recording chamber (chamber volume $\sim$1 mL; perfusion speed $\sim$2 mL/min, total re-circulating volume 20 mL or more) with ACSF-containing calcein (50 μM), we measured a fluorescence signal rapidly arising from the tissue (Figure 2A). The signal originated almost entirely from the ECS, as opposed to cellular structures (Figure 2B). The auto-fluorescence level from the unlabeled tissue was 0.3% of the integrated, normalized ECS intensity after labeling (100%), and levels dropped to $1.5 \pm 0.2\%$ (mean $\pm$ SD, n = 6 imaging areas in 6 slices) after 15 min of wash-out with calcein-free ACSF (Figure 2B). In the same slices, somatic auto-fluorescence was 0.17% before calcein wash-in, reached a maximum of $10 \pm 3\%$ of ECS intensity during wash-in, and dropped to $0.6 \pm 0.3\%$ after wash-out (n = 10 soma, 6 slices; Figure 2B). The somatic fluorescence changed in parallel with ECS fluorescence, indicating it was out-of-focus fluorescence and not of intracellular origin.

We compared bleaching in the intracellular and extracellular compartments, reasoning that bleached fluorophores can be replenished practically forever by diffusion in the ECS, but not inside neurons where the pool of dye molecules is finite. We briefly patch-loaded single neurons with Atto-514 and perfused the ECS with Atto-488 (Figures 2C and 2D). During time-lapse imaging, we observed that the intracellular Atto-514 signal bleached rapidly (significant after 5 frames), while the extracellular Atto-488 signal did not change (n = 8 paired soma from 8 slices,
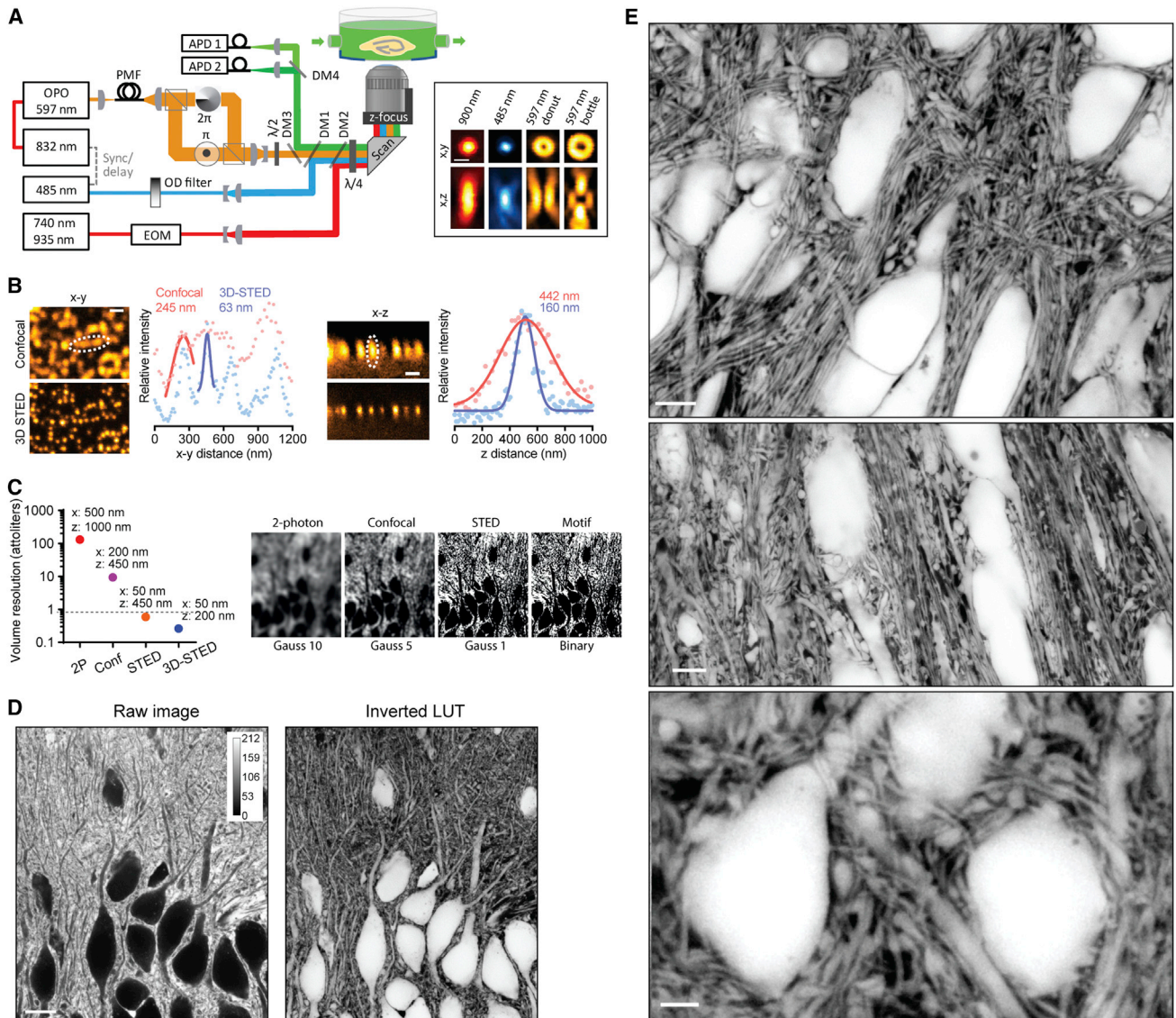
Figure 1. 3D-STED and Extracellular Fluid Labeling for Super-Resolution Shadow Imaging

(A) Left: Schematic of the custom-built microscope used for 3D-STED, confocal, and 2-photon microscopy. Right: PSFs of the different laser beams visualized with 150 nm gold beads. Scale bars in (A), (B), and (C), 500 nm. See also Figure S1.

(B) Fluorescence PSFs measured with 40 nm fluorescent beads, laterally (x-y) and axially (x-z).

(C) Calculated volume resolution (based on an ellipsoid) for different imaging modalities (2P, confocal, STED, 3D-STED) and impact of spatial filtering on image blur.

(D) Raw SUSHI image of hippocampal pyramidal neurons in CA1 stratum oriens (left) and the same image with inverted look-up table (right). Scale bar, 10 μm.

(E) Higher magnification SUSHI images of cell bodies and neuropil in CA1 area. Scale bar in top, 4 μm; middle, 5 μm; bottom, 2 μm. See also Figure S2.

repeated-measures 2-way ANOVA, $F_{[1, 7]} = 12.6$ followed by Sidak's multiple comparisons test; Figure 2E). When the dyes were switched, again only the intracellular signal showed significant bleaching after 3 frames, while the extracellular one remained stable (n = 5 paired soma from 5 slices, repeated-measures 2-way ANOVA, $F_{[1, 4]} = 8.7$, followed by Sidak's multiple comparisons test; Figure 2F).

We also examined the combination of extracellular calcein-green and genetically encoded cytosolic yellow fluorescent protein (YFP). Using the same laser intensities and image acquisition settings as before, the ECS calcein signal showed no decay, while the intracellular YFP signal bleached significantly after 19 frames (n = 9 YFP cell bodies and 10 ECS regions from 8 slices, 2-way ANOVA $F_{[1, 17]} = 10.8$, followed by Sidak's multiple comparisons test; Figure 2G).

Effect of Extracellular Dye on Electrophysiological Neuronal Properties

Even though the dyes we tested for SUSHI are commonly used as innocuous cytosolic labels of live cells, we wanted to find
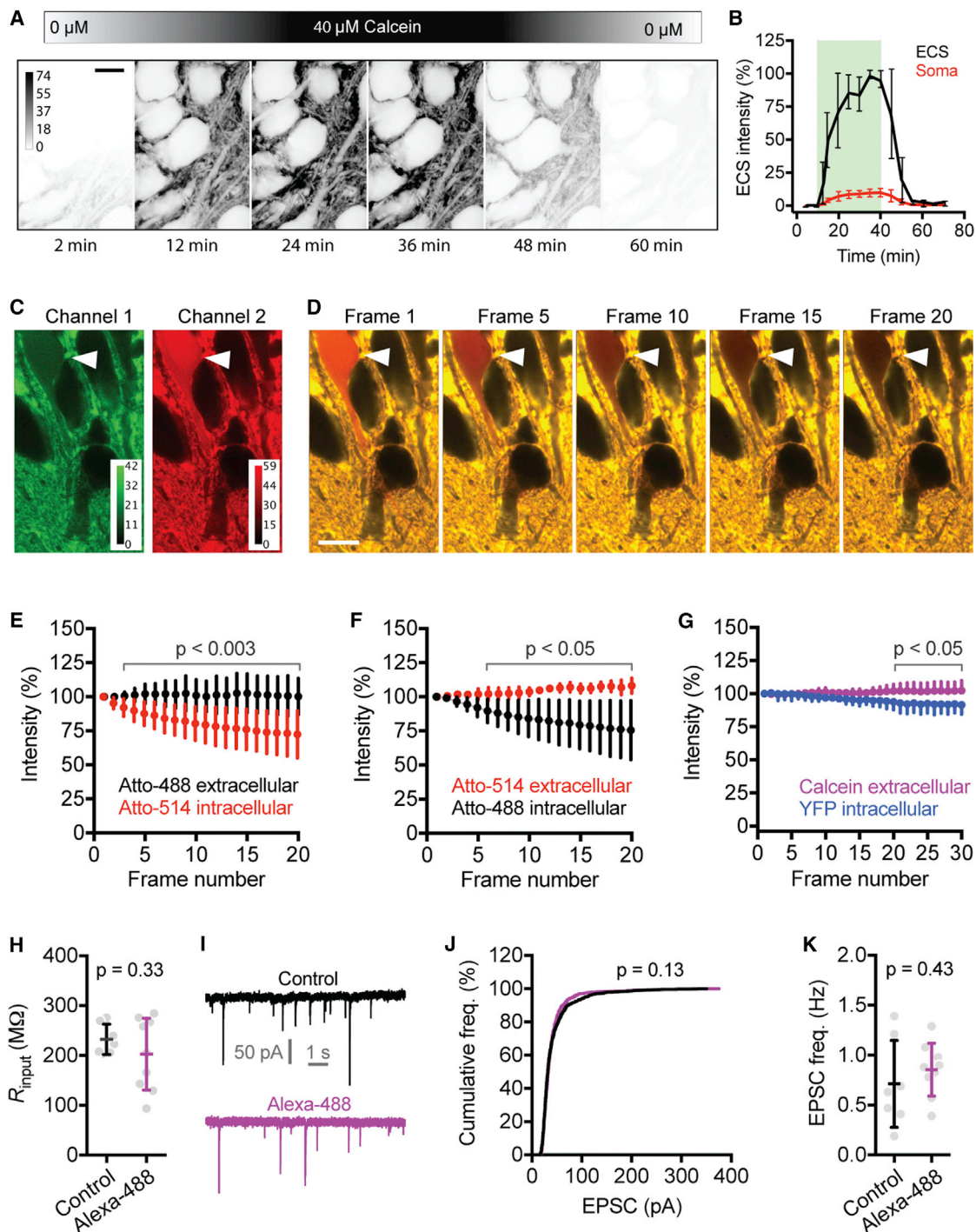
Figure 2. Labeling Strategy Specifically and Reversibly Labels ECS and Is Innocuous to Neurons

(A) Wash-in and wash-out of calcein-green dissolved in the perfusion solution. Scale bar, 10 μm.

(B) Pooled quantification of fluorescence signal during wash-in and wash-out, in soma and ECS compartments (graph depicts mean with SD, n = 6 slices, and n = 10 soma from the same 6 slices, respectively).

(C) Corresponding raw images from simultaneous two-color imaging combining SUSHI with a different intracellular fluorescent dye. The two detection channels are shown in green and red.

(D) Merging the two channels from time-lapse images reveals that only the intracellular label bleached (red cell). Scale bar, 10 μm.

(E) Pooled quantification across experiments, indicating also the outcome of the ANOVA *post hoc* Sidak's multiple comparisons test (data from 8 soma pairs in 8 slices; graph depicts mean with SD).

(legend continued on next page)

out whether their presence in the ECS impacts neuronal function. We whole-cell patched-clamped CA1 neurons during perfusion with control ACSF (n = 7 cells from 7 slices) or ACSF-containing Alexa Fluor 488 (n = 9 cells from 6 slices). We did not detect any significant differences in input resistance (t test p = 0.33; Figure 2H), amplitude of excitatory postsynaptic currents (EPSCs) (n_{Ctr} = 898 EPSCs, $n_{Alexa\ 488}$ = 1089 EPSCs; Kolmogorov-Smirnov test p = 0.13; Figures 2I and 2J), or EPSC frequency (t test p = 0.43; Figure 2K), indicating the absence of any adverse effects of the extracellular labeling strategy on neuronal function.

Estimating ECS Volume Fraction

The high image contrast provided by SUSHI made it possible to estimate the ECS volume fraction ($\alpha = V_{ECS}/V_{total}$) in a straightforward way by binarizing the images: pixels with a signal count above a certain threshold are counted as ECS, while below-threshold pixels represent intracellular space (binary method; Figures 3A and 3B). α is then simply the ratio of the number of above-threshold pixels to the total number of pixels for a given region of interest.

In organotypic brain slices, the binary α ranged from 5% to 36%, with a mean of 19 ± 10% (± SD, n = 15 areas from 10 slices; Figures 3C and 3D), showing wide but consistent regional variations across the CA1 area of the hippocampus, with the smallest values observed in the *stratum pyramidale* (Figure 3C). We also calculated α based on integrated fluorescence intensity levels, dividing the value integrated across the area of interest by the hypothetical maximum if the whole area had been pure ECS (integrative method; Figure S4). While the volume fractions were very strongly correlated between the two methods (linear correlation R^2 = 0.92), the integrative α was higher at 32 ± 6% (mean with SD; paired t test p < 0.001; Figure S4).

Geometric Analysis of ECS Widths

To quantify the width of the interstitial spaces separating neural structures, we analyzed Gaussian fits to the ECS intensity peaks in line profiles measured across the neuropil (n = 620 widths from 9 slices; Figures 3E and 3F). The interstitial spaces were highly heterogeneous, their widths ranging from around 50 nm to well above 1 μm with a positively skewed distribution (minimum = 50 nm, maximum = 3.2 μm, median = 0.27 μm, interquartile range [IQR], 0.13–0.56 μm; Figure 3G). While our microscope cannot resolve structures that are smaller than 50 nm, it should still be able to detect them, assigning them to the 50 nm bin. The vast majority (>80%) of interstitial spaces were larger than 100 nm, which is well within the resolving power of the microscope. By comparison, 2-photon microscopy yielded ECS widths that were significantly larger (median = 0.55 μm,

IQR 0.33–0.96 μm, n = 132 widths from 5 slices; Mann-Whitney test, p < 0.001; Figure S3I).

Hyperosmotic Conditions Cause ECS Expansion

To explore the ability of SUSHI to reveal ECS dynamics, we subjected the slices to an osmotic challenge, temporarily raising the osmolarity of the ACSF solution (from 302 ± 8 to 374 ± 18 mOsm/L; mean ± SD) by the addition of NaCl while taking time-lapse SUSHI images (Figure 4A). We reasoned that hyperosmotic extracellular conditions should draw water molecules from cells to the extracellular compartment and lead to an expansion of the ECS at the expense of cell volumes. Hyperosmotic stress is known to occur during focal cerebral ischemia and edema formation, yet its effects on brain ECS is not well understood (Bourque, 2008).

Indeed, during transient hypertonic conditions, SUSHI revealed a reversible enlargement of the ECS volume (n = 7 areas from 7 slices; ANOVA F[8, 54] = 7.5, followed by Dunnett's multiple comparisons test), as evidenced by an increase in ECS fluorescence intensity to 119 ± 10% of controls (mean with SD), which returned to 102 ± 6% after reperfusion with normal ACSF (Figure 4B). The increase in ECS volume coincided with an increase in ECS widths (Kruskal-Wallis test p < 0.001, followed by Dunn's multiple comparisons test) from median 0.27 μm (IQR 13–43 μm, n = 136 widths from 7 slices) to 0.39 μm (n = 117 widths from 7 slices; IQR 21–69 μm), which returned to 0.28 μm after switching back to isotonic ACSF solution (n = 139 widths from 7 slices; IQR 15–50 μm; Figure 4C).

Epileptiform Discharges Transiently Reduce ECS

Next, to test whether SUSHI can be used to reveal activity-dependent changes in ECS, we examined the effect of epileptiform discharges on ECS structure. Massively synchronized neuronal discharges occur during epileptic seizures and are associated with large ionic currents in neurons and glial cells, which can cause cell-volume changes. Status epilepticus induced by intraperitoneal injections of pilocarpine was previously shown to cause a reduction in the cortical ECS volume fraction in rats, as measured by real-time iontophoresis (Slais et al., 2008). However, the effects of epileptiform discharges on local ECS and neuropil structure remain poorly understood.

We paired time-lapse SUSHI imaging with electrophysiological field potential recordings and induction of epileptiform activity by bath-applying picrotoxin (PTX, 50 μM), which blocks inhibitory GABA$_A$ receptors (Figure 4D). Rapid time-lapse SUSHI imaging revealed that brief epileptiform discharges coincided with a marked drop in ECS fluorescence intensity to 82 ± 18% of controls (n = 9 areas from 9 slices; mean with SD; paired

(F) When the two fluorophores are switched, only the intracellular one bleached (data from 5 soma pairs in 5 slices).

(G) Fluorescent proteins (YFP and GFP) showed less bleaching than synthetic dyes, such as Alexa and Atto (data from 9 YFP filled somas and 10 ECS areas in 8 slices, plotted as mean with SD).

(H) Perfusion of a hippocampal slice with Alexa Fluor 488 did not significantly alter the input resistance of CA1 neurons (n = 7 cells from 7 control slices and 9 cells from 6 Alexa 488 perfused slices. Graph shows mean with SD and outcome of Student's t test).

(I) Excitatory postsynaptic currents (EPSCs) in control conditions and during perfusion with Alexa Fluor 488.

(J) The amplitudes of EPSCs did not differ between the two groups (from the cells analyzed in [H], n = 898 control EPSCs and 1089 Alexa 488 perfusion EPSCs. The p value reports outcome of Kolmogorov-Smirnov test).

(K) EPSC frequency was not different in the Alexa Fluor 488 group (each point is the average of one cell from one slice with SD. Data from the same 7 control cells and 9 Alexa 488 perfused cells as panels [H]–[J]).

A

SUSHI   ECS   Merge

B

VF 11.1%
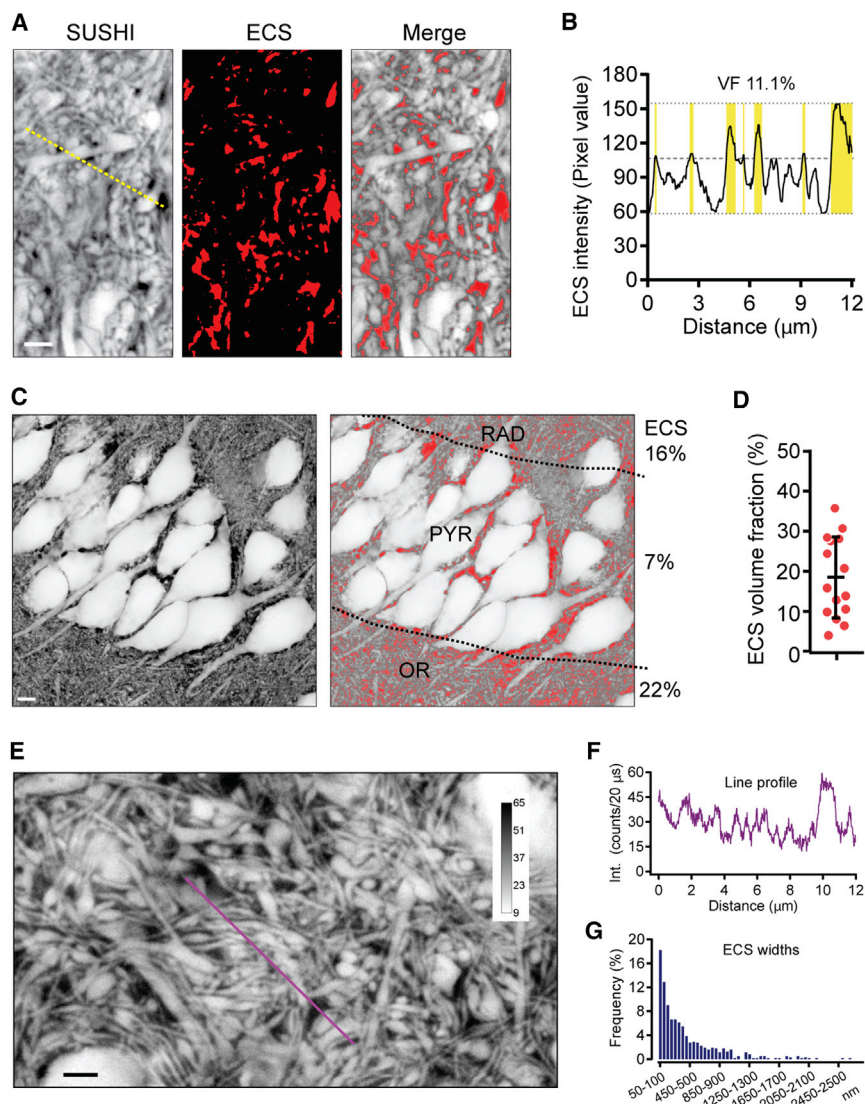
ECS intensity (Pixel value) vs Distance (μm)

Figure 3. Nanoscale Analysis of ECS Volume Fraction and Structure

(A) Raw SUSHI image of neuropil in CA1 *stratum radiatum* (left), the binary image of the ECS volume fraction (left in red), and composite image. Scale bar, 2 μm.

(B) Illustration of the method for calculating the ECS volume fraction based on pixel intensity and thresholding. The plot corresponds to the intensity profile of the yellow line in (A). Yellow areas represent pixels reaching the threshold (dotted line) to be counted as ECS. In this plot, the volume fraction is 11.1%. See also Figure S4.

(C) Overview of CA1 area, illustrating the *oriens*, *stratum pyramidale*, and *stratum radiatum* having different ECS volume fractions. Scale bar, 5 μm.

(D) Estimated hippocampal volume fractions across experiments (each point represents an ECS area, the bar shows mean and SD. n= 15 areas from 10 slices).

(E) Raw SUSHI image of hippocampal neuropil. See also Figures S3E–S3I.

(F) Intensity profile of the lilac line shown in (A). The peaks correspond to areas of ECS, while dips represent neural structures. Scale bar, 2 μm.

(G) Frequency distribution of observed ECS widths across experiments (n = 620 widths from 9 slices).

C

RAD — ECS 16%

PYR — 7%

OR — 22%

D

ECS volume fraction (%)

E

F

Line profile

Int. (counts/20 μs) vs Distance (μm)

G

ECS widths

Frequency (%) vs nm (50-100 ... 2450-2500)

Local Glutamate Release Induces ECS Dynamics

To explore whether SUSHI could detect highly localized activity-driven changes in ECS structure, we examined whether 2-photon glutamate uncaging, mimicking the release of glutamate from single synaptic terminals, could induce discernible changes in ECS structure. Prior to SUSHI imaging, we tuned the power of the 2-photon uncaging laser on individual dendritic spines. We voltage-clampe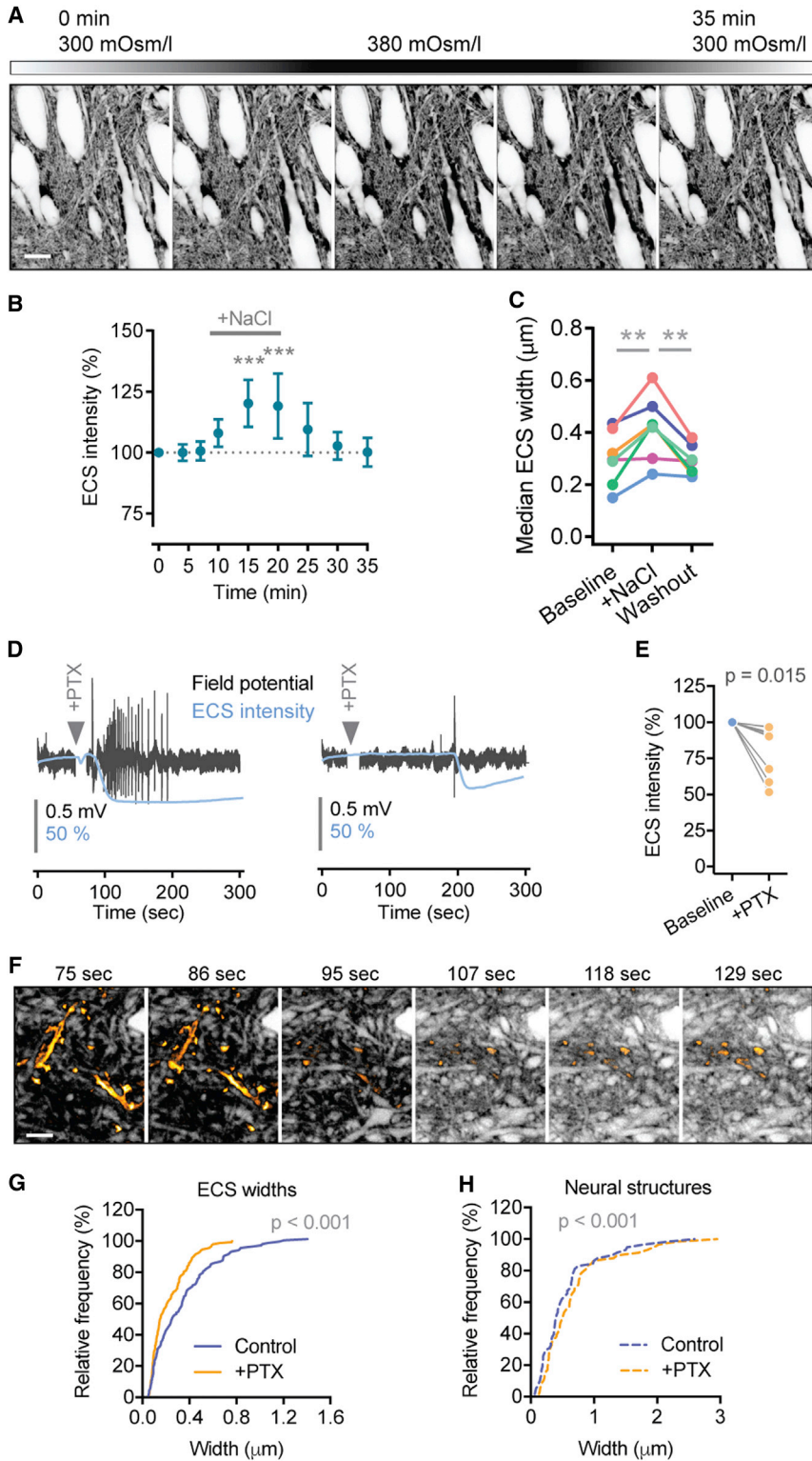d CA1 neurons in whole-cell mode, loaded them with Alexa Fluor 488, and determined the intensity and duration of 2-photon laser pulses that would elicit excitatory postsynaptic currents (uEPSC) resembling physiological EPSCs in duration and amplitude (Figures 5A–5C).

We then labeled the ECS and delivered a series of 30 uncaging pulses to the stratum radiatum (1 Hz, 1 ms pulse-width; Figure 5D), while acquiring time-lapse SUSHI images in rapid succession (0.7 frames per second; Figures 5E and 5F). These conditions are similar to a common protocol to induce postsynaptic plasticity, except we did not remove Mg^{2+} from the ACSF because we wanted to preserve physiological conditions in the extracellular space.

The intensity of the ECS signal averaged over a 1 μm^2 region of interest around the uncaging spot showed a modest but significant drop (n = 18 uncaging areas from 6 slices, repeated-measures 2-way ANOVA, $F_{time}[69, 1173] = 6$, $F_{group}[1, 17] = 7.9$; followed by Sidak's multiple comparisons test), which reached significance 60 s after starting the uncaging

t test p = 0.015; Figure 4D–4F; Movie S1), indicating a decrease in ECS volume. Clustered discharges (Figure 4D, left) tended to induce long-lasting depression of the ECS signal (tens of minutes), whereas single discharges induced more transient changes that recovered within a few minutes, even though the initial drop was comparable (Figure 4D, right).

To verify that these changes indeed reflected ECS shrinkage, we measured the geometric widths of the ECS and neural structures in the SUSHI time-lapse images. We detected a left-shift in the distribution of ECS widths following discharges, from median 0.26 μm (n = 126 widths from 8 slices; IQR 0.12–0.48 μm), to 0.15 μm (n = 148 widths from 8 slices; IQR 0.09–0.31 μm; Mann-Whitney test p < 0.001; Figure 4G). Concurrently, neural structures increased in width from a median of 0.40 μm (IQR 0.20–0.65 μm) to 0.51 μm (IQR 0.28–0.78 μm; both n = 58 widths (paired); Wilcoxon matched pairs test p < 0.001; Figure 4H), indicating that cell swelling constricted the ECS and reduced overall ECS volume.

Figure 4. ECS Dynamics in Response to Osmotic Challenge and Epileptiform Discharges

(A) Time-lapse sequence during a transient hyperosmotic challenge. During the challenge, ECS patches appeared or existing ones became larger around soma, consistent with cell shrinkage. Scale bar, 10 μm.

(B) ECS intensity integrated across individual frames during the hyperosmotic challenge. Each point represents the mean and SD of n = 7 ECS areas from 7 slices. Raising the osmolarity led to an increase in fluorescence, consistent with an increase in ECS volume fraction (asterisks report outcome of Dunnett's *post hoc* test, following an ANOVA).

(C) Measurement of ECS widths across experiments during the hyperosmotic challenge. Each point represents the median width of an area, n = 7 areas from 7 slices and 117 widths (asterisks report result from Kruskal-Wallis followed by Dunn's test). The transient increase in osmolarity triggered a transient increase in ECS width, consistent with cell shrinkage.

(D) Two examples of PTX-induced epileptiform discharges shown together with ECS fluorescence intensity (blue line).

(E) Pooled quantification of the initial drop in fluorescence following electrical discharges (result from paired t test).

(F) Images from two-color time-lapse SUSHI sequence during epileptiform discharges, illustrating the drop in ECS intensity (note that LUT is inverted). Imaging and display parameters were the same across the images. Scale bar, 2 μm. See also Movie S1.

(G) Cumulative distribution of ECS widths during control condition and following PTX-induced discharges reveals shrinkage of the ECS (n = 126 widths from 8 slices. p value is from Mann-Whitney test).

(H) In parallel with ECS shrinkage, neural structures swelled up following discharges (n = 58 widths observed under the two conditions. p value is from Wilcoxon test).
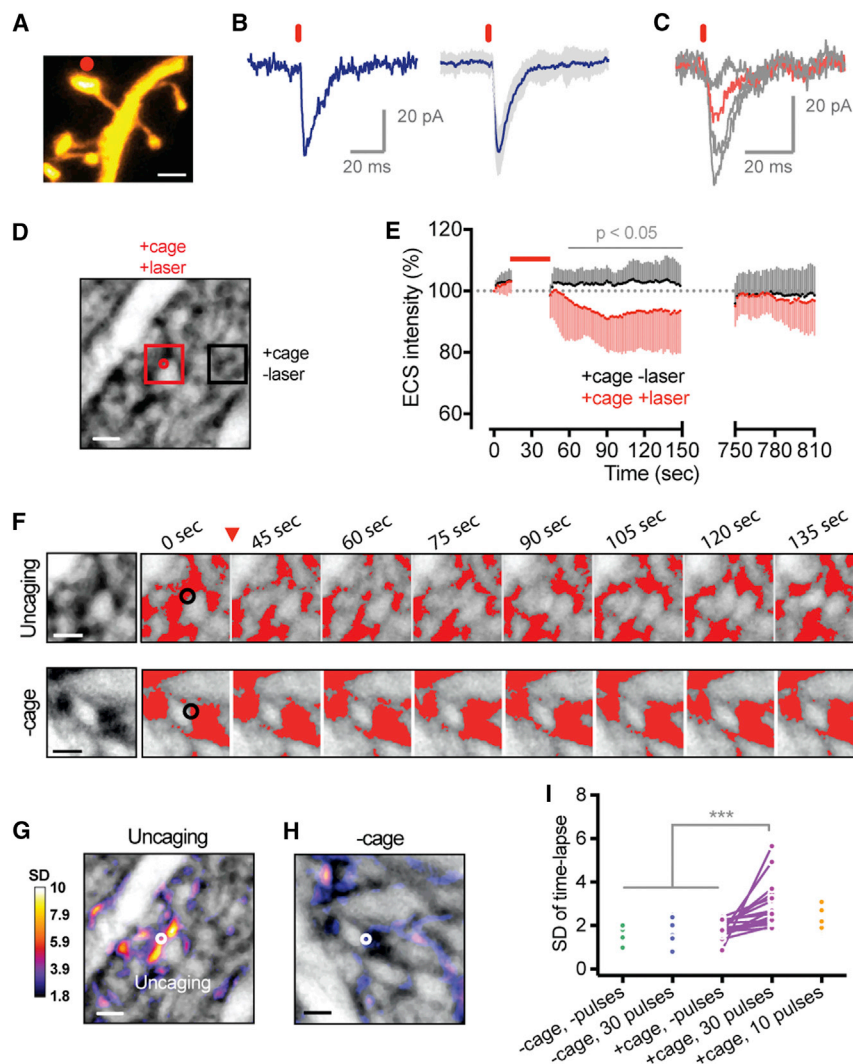
Figure 5. Glutamate Uncaging Induces ECS Remodeling

(A) 3D-STED image of YFP-labeled dendritic spine, with the 2-photon glutamate uncaging spot illustrated in red. Scale bar, 1 μm.

(B) Single trace of electrophysiological response to glutamate uncaging, and average trace based on 20 single-pulse repetitions.

(C) The power of the uncaging laser was varied stepwise, and the lowest power that produced a clear electrophysiological response (in red) was chosen for further uncaging experiments. This was in the range of 2–3 mW at the sample.

(D) SUSHI image indicating the uncaging spot (red dot), the uncaging analysis area (red square), and control analysis area (black square). Scale bar, 1 μm.

(E) Temporal profile of ECS intensity measured in the 1 μm² analysis area (red) and a control area (black) before and after uncaging. Each point is the mean with SD of 18 uncaging areas from 6 slices (p value valid for all points under the gray line is from 2-way ANOVA followed by Sidak's multiple comparisons test).

(F) Zoom-in on the uncaging area and a time-lapse of the same area with the ECS volume fraction superimposed in red, illustrating glutamate-induced local remodeling of the ECS. Scale bar, 1 μm. See also Movie S2.

(G) Pixel-by-pixel SD projection of the time-lapse sequence superimposed on the first image of the time-lapse (corresponding to zoom-in [D]), revealing areas of increased dynamics. Scale bar, 1 μm.

(H) SD projection of time-lapse following 2-photon uncaging in the absence of the caged glutamate. Scale bar, 1 μm.

(I) Pooled quantifications of mean and SD across condition show that the increased temporal dynamics in ECS structure were specific to glutamate uncaging with 30 pulses (n = 18 uncaging areas from 10 slices) and not induced by laser pulses in the absence of the caged glutamate (n = 18 areas from 18 slices) or by only 10 uncaging pulses (n = 9 areas from 9 slices). The latter three did not induce activity above baseline in the absence of both laser and cage (n = 9 areas from 9 slices). Paired data are connected by lines (p value is outcome of ANOVA followed by Tukey's test).

stimulus when compared to controls (or 69 s compared to time point 0, by Dunnett's *post hoc* test) and persisted for several minutes. Fluorescence in neighboring control regions showed no discernible fluorescence change (compared to control time point 0, Dunnett's *post hoc* test; Figure 5E). The maximum fluorescence change occurred around 45 s after uncaging had ceased, corresponding to 91 ± 11% (mean with SD) of the initial intensity at time point 0 (100%).

Revisiting the uncaging areas 10 min later revealed that fluorescence levels had returned to baseline levels and were not different from time point 0 (n = 6 areas from 6 slices, repeated-measures 2-way ANOVA, F_{time}[41, 205] = 1.14, F_{group}[1, 5] = 0.12).

The drop in ECS fluorescence intensity indicates a modest net decrease in ECS volume. However, the time-lapse image data reveal that the ECS was remodeling in a highly dynamic way around the uncaging spot (Figures 5E and 5F; Movie S2). To

quantify the complex dynamics, we calculated the standard deviation of the ECS signal over time for each pixel in the image (Figures 5G and 5H).

The background SD measured across a 1 μm² area in the absence of caged glutamate and uncaging laser was 1.5 ± 0.4 (± SD of the mean SD, n = 9 uncaging areas from 9 slices), reflecting spontaneous ECS fluctuations and measurement noise. This value was not different from the SD of 1.7 ± 0.4 after delivering the 30 uncaging pulses in the absence of the cage (n = 15; Figure 5H), from the 1.8 ± 0.4 SD of delivering the cage without the uncaging pulses (n = 18 areas from 18 slices), or the 2.2 ± 0.5 SD of delivering 10 pulses in the presence of the cage (n = 9 areas from 9 slices; Figure 5I). By contrast, 30 pulses in the presence of the cage significantly increased the SD to 2.9 ± 1.0 (n = 18 areas from 10 slices; ANOVA F[4, 64] = 10.8, followed by Tukey's test; Figure 5I). However, the response to 10 uncaging pulses in the presence of the cage did not differ from the
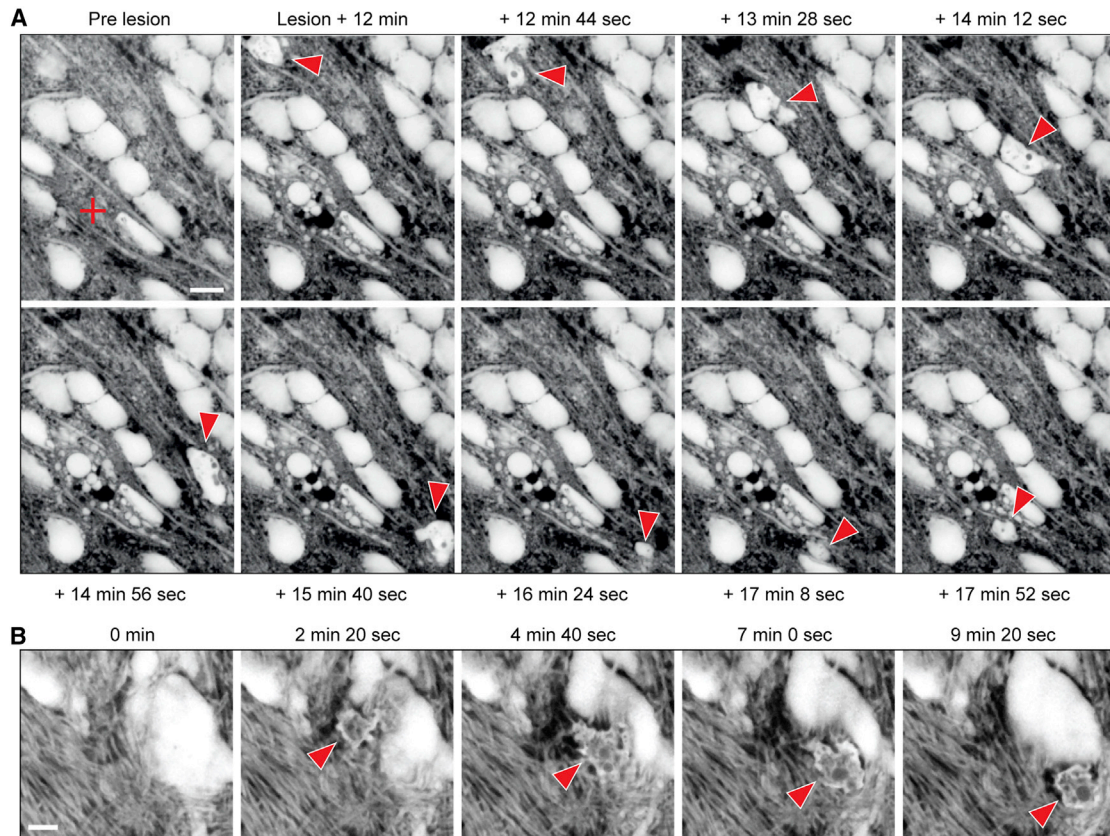
Figure 6. SUSHI Enables Visualization of "Contextualized" Cell Migration

(A) A 2-photon lesion (induced at the cross in first frame) triggered the arrival of a putative microglial cell (red arrow) to the lesion site. Scale bar, 10 μm. See also Movies S3 and S4.

(B) Spontaneous cell migration of a putative microglial cell (red arrow) through bundles of axons. Scale bar, 3 μm. See also Movie S5.

response to 30 pulses (n = 9 areas from 9 slices; ANOVA followed by Tukey's test p = 0.07; Figure 5I).

SUSHI of Cell Migration through Visible Neuropil

Given that neural structures and cells are visualized as inverse images by the extracellular labeling strategy, we set out to monitor cell migration with the benefit of seeing the ECS and neuropil context at the same time.

To induce cell migration, we used 2-photon laser pulses to inflict small lesions in the brain slice, which is known to activate microglial cells. Time-lapse imaging for over 1 hr, we could monitor the arrival and dynamics of putative microglial cells at the lesion site (Figure 6A; Movies S3 and S4). While some cells followed a curvy trajectory through the neuropil to the lesion site, navigating around neuronal cell bodies (Movie S3), other cells ripped straight through it, leaving behind a channel in the ECS (Movie S4).

We also observed episodes of spontaneous cell migration. In one example, a putative microglial cell visibly displaced a cell body and a bundle of axons while moving through the dense neuropil in an amoeboid fashion (Figure 6B; Movie S5). Notably, the cell had taken up dye from the ECS, visible in intracellular vesicles, consistent with the phagocytic capacity of microglial cells.

SUSHI for Anatomical Analysis of Unlabeled Neurons

As SUSHI provides super-resolved negative images of cellular structures, we set out to extract quantifiable information on synaptic structures from unlabeled neurons.

We could frequently observe structural appositions reminiscent of synaptic clefts between dendritic spines and axonal boutons (Figures 7A and 7B). It was also possible to discern putative pre- and postsynaptic structures within individual CA3 thorny excrescences, which form synapses with giant boutons of granule cell mossy fibers (Figures 7C, 7D, and S5). In contrast to conventional labeling approaches, which cannot visualize synaptic clefts, in SUSHI the synaptic cleft is brightly labeled and sandwiched between the non-fluorescent presynaptic bouton and postsynaptic spine, providing much more favorable contrast conditions to detect them.

Next, we examined the capacity of SUSHI to reveal the neuropil surrounding positively labeled neurons, which is practically impossible by regular fluorescence imaging approaches (Figure 7E; Movie S6).

Putative synaptic contacts between YFP-labeled dendritic spines and inversely labeled boutons became visible (Figures 7F and 7G), making it possible to count the number of boutons impinging on a single spine. It also facilitates correlative
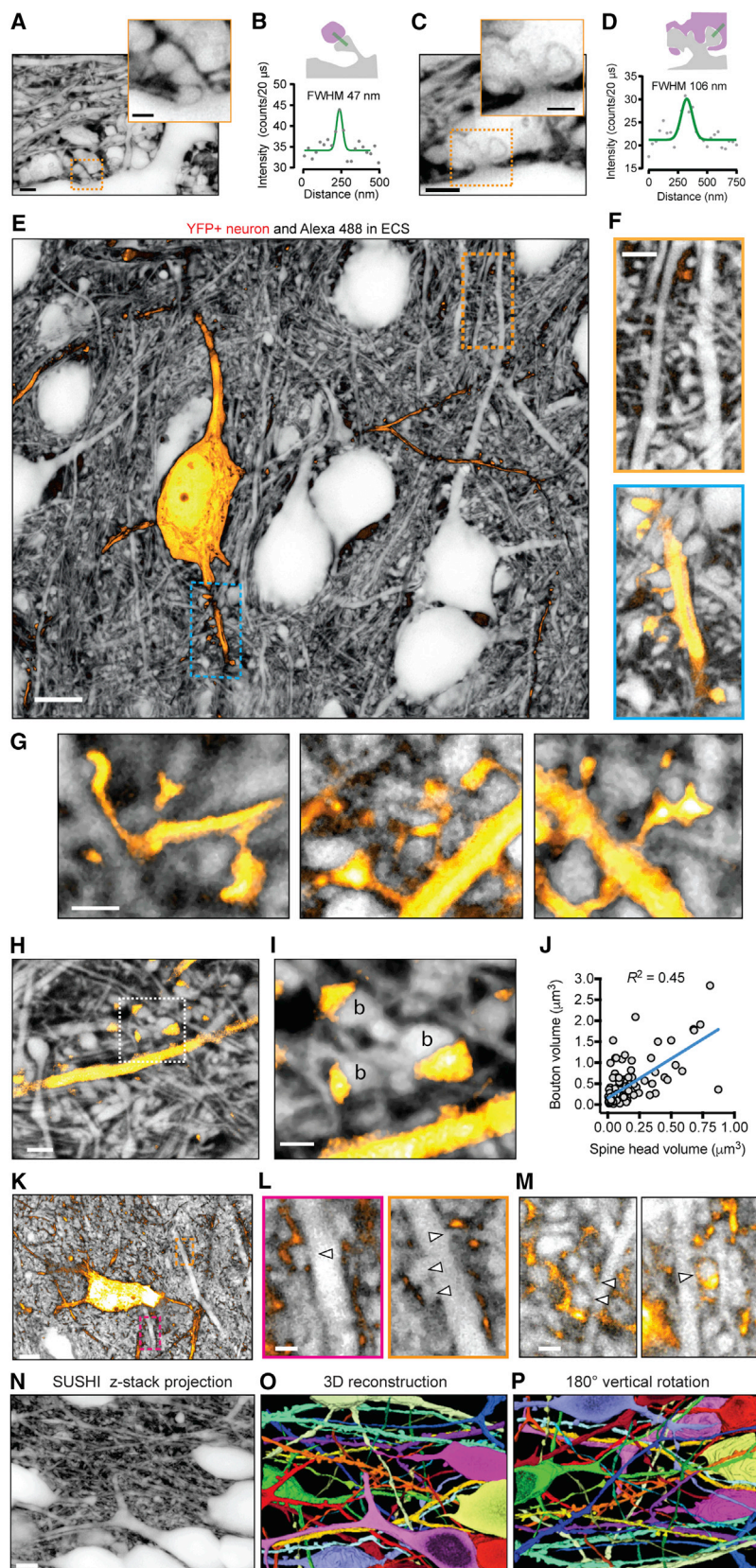
Figure 7. SUSHI for Unbiased Nanoscale Imaging of Cell Morphology

(A) Dendritic spine in contact with presynaptic bouton imaged by SUSHI, revealing a putative synaptic cleft. Scale bar, 2 μm and 1 μm in the zoomed insert.

(B) Line profile across putative synaptic cleft.

(C) Zoom-in on lower left area of frame shown in (A), showing a giant mossy fiber bouton with multi-headed dendritic spines, or thorny excrescence, inside (zoom-in). Scale bar, 2 μm and 1 μm in the zoomed insert. See also Figure S5.

(D) Line profile across putative cleft.

(E) Single-section 2-color SUSHI image, illustrating a cytosolically YFP-labeled CA1 neuron and surrounding neuropil. Note that SUSHI reveals putative cytosolic organelles within the YFP-labeled soma. Scale bar, 10 μm. ECS channel was inverted, but not YFP-channel. See also Movie S6.

(F) Zoom-in on boxed areas in (E), displaying unlabeled dendritic spines imaged by SUSHI (top) and unlabeled presynaptic partners of YFP-labeled dendritic spines (bottom). Scale bar, 2 μm.

(G) YFP-labeled dendritic spines and their unlabeled presynaptic partners. Scale bar, 1 μm.

(H) YFP-labeled dendritic segment and surrounding neuropil. Scale bar, 2 μm.

(I) Zoom-in on boxed area in (H), with three visible spine heads, each with presynaptic boutons, identified by b. Scale bar, 1 μm.

(J) Correlation between volumes of spine heads and the volumes of their respective presynaptic boutons (n = 123 spine/bouton pairs from 5 slices).

(K) ZsGreen-labeled astrocyte in the context of the neuropil imaged by SUSHI. Scale bar, 5 μm.

(L) Zoom-in on boxed areas in (K), with dendritic spines covered by astrocytic process indicated by arrows.

(M) Unlabeled dendritic spines (arrows) that are covered by astrocytic processes. Scale bar, 1 μm.

(N) Minimum intensity projection through a 30-section SUSHI z stack spanning 5.8 μm. Scale bar, 5 μm.

(O) 3D reconstruction of 26 cellular structures from the stack displayed in (N). See also Figure S7 and Movie S7.

(P) The same 3D reconstructed volume rotated 180° vertically.

anatomical analysis of pre- and postsynaptic structures (Figures 7H and 7I), allowing us to reveal a strong correlation between the volumes of presynaptic boutons and dendritic spines (n = 123 synapses from 5 slices; linear regression R^2 = 0.45); Figure 7J).

We next tested whether morphological parameters reported by SUSHI agree with those obtained by STED of positively labeled structures. We quantified inversely labeled axon shafts, which had a median width of 242 nm (IQR 181–352 nm; n = 57 axons from 7 slices), which was not different from the width of 237 nm (IQR 190–299 nm; n = 66 axons from 6 slices) from positively labeled axons in the same brain slices (Mann-Whitney test p = 0.72; Figures S6A–S6D).

In addition to neurons, we positively labeled astrocytes and visualized the neuropil around them, revealing dendritic spines in close contact with hyperfine astrocytic processes, forming putative tripartite synapses (Araque et al., 1999), which are beyond the resolution of regular light microscopy (Figures 7K–7M) (Panatier et al., 2014).

SUSHI of Intracellular Spaces and Structures

While we have primarily explored SUSHI in the context of the ECS, it can also be used to survey the intracellular space of cytosolically labeled cells. Imaging YFP-expressing neurons with 3D-STED clearly demarcated silhouettes of spherical and reticular structures, presumably representing cellular organelles, such as nucleoli, endoplasmic reticulum and Golgi apparatus (YFP-labeled cell in Figure 7E; Figure S6E). In contrast to conventional strategies, which target specific molecules or compartments, SUSHI reveals the spatial relationships of intracellular structures from a more global and unbiased vantage point and without the need for labeling them.

Morphological 3D Reconstructions of Unlabeled Neurons Imaged by SUSHI

Finally, we explored the possibility of using SUSHI to trace individual unlabeled cellular structures and reconstruct them in 3D. We could readily reconstruct more than 50% of a given imaged volume, producing detailed views of the spatial relationships of anatomical structures like axons and dendrites, whose spinous morphology could be well resolved (Figures 7O–7Q and S7; Movie S7).

DISCUSSION

We introduce SUSHI to reveal the spatial organization and dynamics of the ECS in living brain tissue with sub-diffraction spatial resolution and high image contrast, providing a straightforward light microscopic alternative to EM and biophysical techniques for studying brain ECS. It hinges on the attoliter volume resolution of 3D-STED microscopy in combination with labeling of the extracellular fluid by a diffusible, membrane-impermeant fluorescent marker, which together add up to a major advance in the ability to visualize brain tissue.

Labeling the space outside of cells has been used before, e.g., for measuring the speed of red blood cells in brain capillaries (Kleinfeld et al., 1998), for determining volume changes in cell lines during osmotic challenges (Droste et al., 2005) and for visualizing cell bodies for targeted patch-clamp recordings by 2-photon microscopy in the mouse cortex *in vivo* (Kitamura et al., 2008). However, shadow imaging has never been applied to reveal brain ECS or to analyze synaptic structures.

Since the ECS is essentially the negative imprint of all cellular structures, SUSHI enables concurrent imaging of brain ECS and brain parenchyma. Revealing *all* cellular structures in one simple labeling step sets SUSHI apart from intracellular labeling schemes, which are inherently more invasive, biased toward a particular cell population, and much less efficient at generating morphological contrast, because the intracellular space is so much larger than the ECS.

Another notable advantage over intracellular labeling is the insensitivity of SUSHI to photobleaching that allows extensive 3D-STED time-lapse imaging of large fields of view. Furthermore, SUSHI also stands to be impacted less by phototoxicity, as any potentially phototoxic molecules are produced outside of the cells from where they wash away quickly, and the extended super-resolution time-lapse series presented here testify to this benefit.

From a practical point of view, labeling can be acutely and reversibly adjusted on the fly. Essentially any fluorophore that is used for intracellular labeling can be applied for SUSHI, including inexpensive calcein. Similarly, fluorophores that are commonly used for multi-color imaging are bound to be suitable for multi-color SUSHI of ECS and cellular compartments.

The reported range of ECS volume fractions is in line with previously published values for cortical brain tissue based on iontophoretic measurements (Lehmenkühler et al., 1993) and cryoelectron microscopy (cryo-EM) (Korogod et al., 2015). Furthermore, our results agree well with cell-layer-dependent variations in ECS volume fraction reported for hippocampal brain slices (McBain et al., 1990).

We demonstrated that the ECS in organotypic slices feature widths that are broadly and lognormally distributed, the majority being between 100 nm and 300 nm, which warrants the super-resolution approach over conventional light microscopy. This distribution is in excellent agreement with recent measurements in acute brain slices based on cryo-EM (Korogod et al., 2015) and tracking of carbon nanotubes (Godin et al., 2017). Whether ECS widths are similar *in vivo* remains to be determined, but recent measurements reporting volume fractions of up to 24% in the cortex of living mice suggest so (Xie et al., 2013).

SUSHI revealed frequent reservoirs of ECS next to cell bodies. These could reflect liquid-filled voids in the neuropil or contain specialized extracellular matrix structures, such as perineuronal nets (PNN). PNNs wrap around certain neurons and are thought to regulate neural plasticity (reviewed in Sorg et al. (2016)), with the pattern of holes in the PNN proposed to store long-term memories (Tsien, 2013). Correlating SUSHI with markers of the extracellular matrix, such as Hapln1 and MMP9 (Senkov et al., 2014), will facilitate the study of the structure and function of PNNs. The fact that a 10 kDa fluorophore could label these spaces suggests a relatively permeable structure.

To our knowledge, dynamic changes in ECS structure have never been visualized. Our time-lapse imaging experiments document distinct structural changes in ECS in response to a variety of physiologically relevant stimuli, indicating that ECS dynamics are a common physiological phenomenon, which may affect brain physiology in several ways.

Global changes, as we could observe after changing ECS osmolarity, are likely to reflect osmotic transients and passive cell-volume changes. Interestingly, the fast and large decrease in ECS volume fraction observed after epileptiform discharges returned back to baseline only very slowly. If interictal events can indeed change ECS volume in a long-term way, this may substantially affect circuit excitability and epileptogenesis.

Notably, glutamate release that mimicked the activity of single synapses elicited measurable changes in ECS structure. These dynamics did not reflect simple osmotic re-equilibration as they had a delayed onset and were fluctuating in time. It is conceivable that glutamate attracts glial processes that contribute to neurotransmitter clearance or that serve other activity-dependent roles (Zheng and Rusakov, 2015), which can be explored in future studies combining SUSHI with positive labeling of glial cells. It seems inevitable that ECS structural changes around synapses will influence synaptic function, for instance by modulating glial uptake of K^+ and glutamate as well as neurotransmitter spillover.

Activity-dependent changes in ECS structure could provide an important control mechanism for regulating circuit function on multiple spatial and temporal scales.

Recent studies have proposed the existence of a "glymphatic" system in the brain, in which structural changes in the ECS are hypothesized to regulate the flow of cerebrospinal fluid and the clearance of metabolites during sleep (Ding et al., 2016; Xie et al., 2013). Moreover, it is likely that ECS structure and dynamics are altered during brain pathology, such as astrogliosis following traumatic brain injury and stroke. However, the extent and nature of ECS structural changes associated with various (patho-) physiological brain states remain largely unknown. SUSHI now provides a powerful means of addressing such questions.

In parallel to visualizing the ECS, SUSHI provides detailed yet panoramic views of live brain parenchyma, reminiscent of zoomed-out ultrastructural EM images but having the benefit of a live tissue setting.

Hence, SUSHI enables unbiased nanoscale imaging of unlabeled cells, revealing spatial relationships and anatomical interactions that remain inaccessible for existing microscopy approaches. Seeing individual cells and their anatomical context is particularly valuable for brain tissue, which has a uniquely complex spatial organization, both at the cellular and network level, where 1 cubic millimeter of brain tissue is estimated to contain 100,000 neurons and 4 km of axon wires (Braitenberg, 1991; Herculano-Houzel, 2009).

We used SUSHI to analyze axons and synaptic structures such as boutons in contact with positively labeled dendritic spines. Axon widths assessed by SUSHI and regular STED imaging were indistinguishable and agreed well with published values (Chéreau et al., 2017; Shepherd and Harris, 1998). SUSHI enabled comparisons of live pre- and postsynaptic hippocampal structures and revealed a strong correlation between sizes of axonal boutons in contact with dendritic spines, which validates previous EM results from fixed tissue (Holderith et al., 2012).

Notably, due to the high contrast of the inverse cellular labeling, SUSHI can directly visualize putative synaptic clefts, paving the way for quantifying potential changes in their structure and dynamics during synapse development and activity-dependent synaptic plasticity. This substantially improves on previous super-resolution analyses of synaptic clefts that rely on labeling of pre- and postsynaptic proteins and multicolor imaging in fixed tissue sections (Dani et al., 2010). Finally, we demonstrate the capacity of SUSHI to generate high-quality 3D reconstructions of dendritic morphology and to trace unlabeled neuronal processes, thereby adding to brain connectomics approaches based on EM, fluorescence microscopy, and magnetic resonance imaging (MRI) (Cazemier et al., 2016; Helmstaedter, 2013; Jbabdi et al., 2015).

Moreover, SUSHI makes it possible to observe "contextualized cell migration," where the migrating cell and the surrounding neuropil are simultaneously visible. It thus greatly increases the chance to observe rare or unexpected events and short-lived interactions between different cellular players. For instance, SUSHI may make it possible to observe directly "synaptic stripping" (Kettenmann et al., 2013), which is hypothesized to contribute to remodeling of synaptic circuits (Hong et al., 2016; Pfeiffer et al., 2016) but has remained elusive.

Together with super-resolution imaging, the inverse labeling strategy can also unveil subcellular organelles in volume-filled cells and provides a minimally invasive, *ad hoc* way to image the morphology of naive dissociated neurons.

In the near future, SUSHI should be applicable *in vivo* like regular STED microscopy by using the standard cranial window approach and an upright 3D-STED microscope. The main challenges are similar to regular STED microscopy: imaging depth and brain motion. Here, we applied SUSHI to a tissue depth of around 50 μm, which would already give access to cortical layer 1 *in vivo*. The use of adaptive optics (Gould et al., 2012; Patton et al., 2016) and 2-photon STED microscopy (Bethge et al., 2013; Takasaki et al., 2013) is likely to enable deeper imaging for SUSHI. Optimized surgery and anesthesia techniques, in addition to higher ECS dye concentrations, which allow faster scan speeds, are bound to reduce motion artifacts to manageable levels.

In summary, SUSHI opens up a new paradigm for live-cell super-resolution imaging of complex and dense biological tissue, which complements and extends conventional approaches based on intracellular labeling. As a versatile fluorescence imaging technique, it opens up manifold experimental opportunities to study the physiology of brain ECS and cellular structure in health and disease.

STAR★METHODS

Detailed methods are provided in the online version of this paper and include the following:

- KEY RESOURCES TABLE
- CONTACT FOR REAGENT AND RESOURCE SHARING
- EXPERIMENTAL MODEL AND SUBJECT DETAILS
  - Experimental animals
  - Mouse lines used for organotypic hippocampal cultures
  - Rat line used for dissociated cell culture
- METHOD DETAILS
  - Organotypic slices of hippocampus
  - Primary hippocampal neuron culture

- ○ 3D-STED microscope
- ○ Extracellular labeling and imaging
- ○ Electrophysiological whole-cell and field recordings
- ○ Analyzing ECS width and volume fraction
- ○ Hyper-osmolarity challenge
- ○ Epileptiform activity
- ○ Two-photon glutamate uncaging
- ○ Two-photon laser lesions
- ○ Image processing
- ○ 3D reconstructions
- ● QUANTIFICATION AND STATISTICAL ANALYSIS

SUPPLEMENTAL INFORMATION

Supplemental Information includes seven figures and seven movies and can be found with this article online at https://doi.org/10.1016/j.cell.2018.02.007.

AUTHOR CONTRIBUTIONS

Conceptualization, U.V.N.; Methodology, J.T., V.V.G.K.I., and U.V.N.; Investigation, J.T. and V.V.G.K.I.; Formal Analysis and Visualization, J.T. and U.V.N.; Writing – Original Draft and Review & Editing, J.T. and U.V.N.; Supervision, U.V.N.

DECLARATION OF INTERESTS

The authors declare no competing interests.

REFERENCES

Araque, A., Parpura, V., Sanzgiri, R.P., and Haydon, P.G. (1999). Tripartite synapses: glia, the unacknowledged partner. Trends Neurosci. 22, 208–215.

Berning, S., Willig, K.I., Steffens, H., Dibaj, P., and Hell, S.W. (2012). Nanoscopy in a living mouse brain. Science 335, 551.

Bethge, P., Chéreau, R., Avignone, E., Marsicano, G., and Nägerl, U.V. (2013). Two-photon excitation STED microscopy in two colors in acute brain slices. Biophys. J. 104, 778–785.

Bourque, C.W. (2008). Central mechanisms of osmosensation and systemic osmoregulation. Nat. Rev. Neurosci. 9, 519–531.

Braitenberg, V., and Schüz, A. (1991). Anatomy of the cortex: statistics and geometry (Springer: Springer Berlin Heidelberg).

Cazemier, J.L., Clascá, F., and Tiesinga, P.H. (2016). Connectomic Analysis of Brain Networks: Novel Techniques and Future Directions. Front. Neuroanat. 10, 110.

Chéreau, R., Saraceno, G.E., Angibaud, J., Cattaert, D., and Nägerl, U.V. (2017). Superresolution imaging reveals activity-dependent plasticity of axon morphology linked to changes in action potential conduction velocity. Proc. Natl. Acad. Sci. USA 114, 1401–1406.

Dani, A., Huang, B., Bergan, J., Dulac, C., and Zhuang, X. (2010). Super-resolution imaging of chemical synapses in the brain. Neuron 68, 843–856.

Danzl, J.G., Sidenstein, S.C., Gregor, C., Urban, N.T., Ilgen, P., Jakobs, S., and Hell, S.W. (2016). Coordinate-targeted fluorescence nanoscopy with multiple off states. Nat. Photonics 10, 122–128.

Ding, F., O'Donnell, J., Xu, Q., Kang, N., Goldman, N., and Nedergaard, M. (2016). Changes in the composition of brain interstitial ions control the sleep-wake cycle. Science 352, 550–555.

Droste, M.S., Biel, S.S., Terstegen, L., Wittern, K.P., Wenck, H., and Wepf, R. (2005). Noninvasive measurement of cell volume changes by negative staining. J. Biomed. Opt. 10, 064017.

Gähwiler, B.H. (1988). Organotypic cultures of neural tissue. Trends Neurosci. 11, 484–489.

Gähwiler, B.H., Capogna, M., Debanne, D., McKinney, R.A., and Thompson, S.M. (1997). Organotypic slice cultures: a technique has come of age. Trends Neurosci. 20, 471–477.

Godin, A.G., Varela, J.A., Gao, Z., Danné, N., Dupuis, J.P., Lounis, B., Groc, L., and Cognet, L. (2017). Single-nanotube tracking reveals the nanoscale organization of the extracellular space in the live brain. Nat. Nanotechnol. 12, 238–243.

Gould, T.J., Burke, D., Bewersdorf, J., and Booth, M.J. (2012). Adaptive optics enables 3D STED microscopy in aberrating specimens. Opt. Express 20, 20998–21009.

Harris, K.M., and Stevens, J.K. (1989). Dendritic spines of CA 1 pyramidal cells in the rat hippocampus: serial electron microscopy with reference to their biophysical characteristics. J. Neurosci. 9, 2982–2997.

Helmstaedter, M. (2013). Cellular-resolution connectomics: challenges of dense neural circuit reconstruction. Nat. Methods 10, 501–507.

Herculano-Houzel, S. (2009). The human brain in numbers: a linearly scaled-up primate brain. Front. Hum. Neurosci. 3, 31.

Hirrlinger, P.G., Scheller, A., Braun, C., Hirrlinger, J., and Kirchhoff, F. (2006). Temporal control of gene recombination in astrocytes by transgenic expression of the tamoxifen-inducible DNA recombinase variant CreERT2. Glia 54, 11–20.

Holderith, N., Lorincz, A., Katona, G., Rózsa, B., Kulik, A., Watanabe, M., and Nusser, Z. (2012). Release probability of hippocampal glutamatergic terminals scales with the size of the active zone. Nat. Neurosci. 15, 988–997.

Hong, S., Dissing-Olesen, L., and Stevens, B. (2016). New insights on the role of microglia in synaptic pruning in health and disease. Curr. Opin. Neurobiol. 36, 128–134.

Jbabdi, S., Sotiropoulos, S.N., Haber, S.N., Van Essen, D.C., and Behrens, T.E. (2015). Measuring macroscopic brain connections in vivo. Nat. Neurosci. 18, 1546–1555.

Kaech, S., and Banker, G. (2006). Culturing hippocampal neurons. Nat. Protoc. 1, 2406–2415.

Kettenmann, H., Kirchhoff, F., and Verkhratsky, A. (2013). Microglia: new roles for the synaptic stripper. Neuron 77, 10–18.

Kitamura, K., Judkewitz, B., Kano, M., Denk, W., and Häusser, M. (2008). Targeted patch-clamp recordings and single-cell electroporation of unlabeled neurons in vivo. Nat. Methods 5, 61–67.

Kleinfeld, D., Mitra, P.P., Helmchen, F., and Denk, W. (1998). Fluctuations and stimulus-induced changes in blood flow observed in individual capillaries in layers 2 through 4 of rat neocortex. Proc. Natl. Acad. Sci. USA 95, 15741–15746.

Korogod, N., Petersen, C.C., and Knott, G.W. (2015). Ultrastructural analysis of adult mouse neocortex comparing aldehyde perfusion with cryo fixation. eLife 4, e05793.

Lehmenkühler, A., Syková, E., Svoboda, J., Zilles, K., and Nicholson, C. (1993). Extracellular space parameters in the rat neocortex and subcortical white matter during postnatal development determined by diffusion analysis. Neuroscience 55, 339–351.

Lei, Y., Han, H., Yuan, F., Javeed, A., and Zhao, Y. (2017). The brain interstitial system: Anatomy, modeling, in vivo measurement, and applications. Prog. Neurobiol. 157, 230–246.

Lenz, M.O., Sinclair, H.G., Savell, A., Clegg, J.H., Brown, A.C., Davis, D.M., Dunsby, C., Neil, M.A., and French, P.M. (2014). 3-D stimulated emission depletion microscopy with programmable aberration correction. J. Biophotonics 7, 29–36.

McBain, C.J., Traynelis, S.F., and Dingledine, R. (1990). Regional variation of extracellular space in the hippocampus. Science 249, 674–677.

Nägerl, U.V., Willig, K.I., Hein, B., Hell, S.W., and Bonhoeffer, T. (2008). Live-cell imaging of dendritic spines by STED microscopy. Proc. Natl. Acad. Sci. USA 105, 18982–18987.

Nicholson, C., and Hrabětová, S. (2017). Brain extracellular space: the final frontier of neuroscience. Biophys. J. 113, 2133–2142.

Panatier, A., Arizono, M., and Nägerl, U.V. (2014). Dissecting tripartite synapses with STED microscopy. Philos. Trans. R. Soc. Lond. B Biol. Sci. 369, 20130597.

Patton, B.R., Burke, D., Owald, D., Gould, T.J., Bewersdorf, J., and Booth, M.J. (2016). Three-dimensional STED microscopy of aberrating tissue using dual adaptive optics. Opt. Express 24, 8862–8876.

Pfeiffer, T., Avignone, E., and Nägerl, U.V. (2016). Induction of hippocampal long-term potentiation increases the morphological dynamics of microglial processes and prolongs their contacts with dendritic spines. Sci. Rep. 6, 32422.

Senkov, O., Andjus, P., Radenovic, L., Soriano, E., and Dityatev, A. (2014). Neural ECM molecules in synaptic plasticity, learning, and memory. Prog. Brain Res. 214, 53–80.

Shepherd, G.M., and Harris, K.M. (1998). Three-dimensional structure and composition of CA3–>CA1 axons in rat hippocampal slices: implications for presynaptic connectivity and compartmentalization. J. Neurosci. 18, 8300–8310.

Slais, K., Vorisek, I., Zoremba, N., Homola, A., Dmytrenko, L., and Sykova, E. (2008). Brain metabolism and diffusion in the rat cerebral cortex during pilocarpine-induced status epilepticus. Exp. Neurol. 209, 145–154.

Sorg, B.A., Berretta, S., Blacktop, J.M., Fawcett, J.W., Kitagawa, H., Kwok, J.C., and Miquel, M. (2016). Casting a Wide Net: Role of Perineuronal Nets in Neural Plasticity. J. Neurosci. 36, 11459–11468.

Syková, E., and Nicholson, C. (2008). Diffusion in brain extracellular space. Physiol. Rev. 88, 1277–1340.

Takasaki, K.T., Ding, J.B., and Sabatini, B.L. (2013). Live-cell superresolution imaging by pulsed STED two-photon excitation microscopy. Biophys. J. 104, 770–777.

Thorne, R.G., and Nicholson, C. (2006). In vivo diffusion analysis with quantum dots and dextrans predicts the width of brain extracellular space. Proc. Natl. Acad. Sci. USA 103, 5567–5572.

Tønnesen, J., Katona, G., Rózsa, B., and Nägerl, U.V. (2014). Spine neck plasticity regulates compartmentalization of synapses. Nat. Neurosci. 17, 678–685.

Tønnesen, J., Nadrigny, F., Willig, K.I., Wedlich-Söldner, R., and Nägerl, U.V. (2011). Two-color STED microscopy of living synapses using a single laser-beam pair. Biophys. J. 101, 2545–2552.

Tsien, R.Y. (2013). Very long-term memories may be stored in the pattern of holes in the perineuronal net. Proc. Natl. Acad. Sci. USA 110, 12456–12461.

Urban, N.T., Willig, K.I., Hell, S.W., and Nägerl, U.V. (2011). STED nanoscopy of actin dynamics in synapses deep inside living brain slices. Biophys. J. 101, 1277–1284.

Van Harreveld, A., and Steiner, J. (1970). The magnitude of the extracellular space in electron micrographs of superficial and deep regions of the cerebral cortex. J. Cell Sci. 6, 793–805.

Vanharreveld, A., Crowell, J., and Malhotra, S.K. (1965). A study of extracellular space in central nervous tissue by freeze-substitution. J. Cell Biol. 25, 117–137.

Wildanger, D., Medda, R., Kastrup, L., and Hell, S.W. (2009). A compact STED microscope providing 3D nanoscale resolution. J. Microsc. 236, 35–43.

Xie, L., Kang, H., Xu, Q., Chen, M.J., Liao, Y., Thiyagarajan, M., O'Donnell, J., Christensen, D.J., Nicholson, C., Iliff, J.J., et al. (2013). Sleep drives metabolite clearance from the adult brain. Science 342, 373–377.

Zheng, K., and Rusakov, D.A. (2015). Efficient integration of synaptic events by NMDA receptors in three-dimensional neuropil. Biophys. J. 108, 2457–2464.

STAR★METHODS

KEY RESOURCES TABLE

REAGENT or RESOURCE	SOURCE	IDENTIFIER
Biological Samples		
Organotypic hippocampal cultures from mouse lines described below	This paper	N/A
Chemicals, Peptides, and Recombinant Proteins		
Eagle's basal medium	ThermoFisher Scientific	Cat#41010-026
Horse serum	ThermoFisher Scientific	Cat#26050088
Hank's balanced salt solution	ThermoFisher Scientific	Cat#14025050
Alexa Fluor 488 hydrazide	ThermoFisher Scientific	Cat#A10436
Dextran, Alexa Fluor 488; 10,000 MW	ThermoFisher Scientific	Cat#D22910
FluoSpheres Microspheres, 0.04 μm, yellow-green fluorescent (505/515)	ThermoFisher Scientific	Cat#F8795
Calcein, high purity	ThermoFisher Scientific	Cat#C481
Atto-514 carboxy	Atto Tec	Cat#AD 514-21
Atto-488 carboxy	Atto Tec	Cat#AD 488-21
Picrotoxin (PTX)	Ascent Scientific	Cat#Asc-315
Tetrodotoxin (TTX)	Ascent Scientific	Cat#Asc-055
QX-314	Ascent Scientific	Cat#Asc-117
Caged glutamate	Femtonics	DNI-Glu-TFA
Experimental Models: Cell Lines		
Primary hippocampal neurons from Sprague Dawley rats	This paper	N/A
Experimental Models: Organisms/Strains		
Mouse/Thy1-YFP-H	Jackson Labs	003782
Mouse/C57BL/6J	Jackson Labs	000664
Mouse/GFAP-cre	Jackson Labs	4418665
Mouse/Ai6 (RCL-ZsGreen)	Jackson Labs	007906
Rat/Sprague-Dawley	Janvier Labs	RjHan:SD
Software and Algorithms		
Imspector data acquisition software	Abberior Instruments	http://www.abberior-instruments.com
ImageJ	NIH	https://imagej.nih.gov/ij
Prism statistical analysis software	Graphpad	https://www.graphpad.com
IGOR Pro data analysis software	WaveMetrics	https://www.wavemetrics.com
Other		
Vortex 2π phase mask	RPC Photonics	Vpp-1a
Annular π delay phase mask	Volker Westphal (MPI, Göttingen)	N/A
Avalanche photodiode	PerkinElmer	SPCM-AQRH-14-FC
Single-mode optical fiber	Schäfter & Kirchhoff	PMC-E-630-4.6-NA011-3-OPC.EC/OPC-2000-P
Pulsed laser diode	PicoQuant	LDH-D-C-485
Optical parametric oscillator	APE	APE OPO Ring fs RTP
Femtosecond laser	Spectra-Physics	MaiTai HP
Laser scan head	ThermoFisher Scientific	Yanus 4 (TILL Photonics)
Patch-clamp amplifier	Molecular Devices	MultiClamp 700B Amplifier

CONTACT FOR REAGENT AND RESOURCE SHARING

Further information and requests for resources and reagents should be directed to and will be provided by the Lead Contact, U. Valentin Nägerl (valentin.nagerl@u-bordeaux.fr).

EXPERIMENTAL MODEL AND SUBJECT DETAILS

Experimental animals

All experiments were performed on mouse organotypic hippocampal slice cultures, with the exception of the data of Figure S3C that were obtained from dissociated rat hippocampal neurons. Experimental procedures were in accordance with the French National Code of Ethics on Animal Experimentation and approved by the Committee of Ethics of Bordeaux. All procedures were in accordance with the guidelines of the European Directive 2010/63/UE.

Mice were housed under 12 h light/12 h dark cycles at 20 to 22°C with *ad libitum* access to food and water in the animal facility of the Inserm Neurocenter Magendie at the University of Bordeaux, and monitored daily by trained staff. All animals used were free of any disease or infection at the time of experiments. Pregnant females and females with litters were kept in cages with one male. We did not distinguish between males and females among the perinatal pups used for organotypic cultures, as potential anatomical and/or physiological differences between the two sexes were considered irrelevant in the context of evaluating the SUSHI approach for imaging the extracellular space. No animals used had been involved in previous experiments.

Mouse lines used for organotypic hippocampal cultures

Organotypic cultures were established from postnatal day 5 to 7 mice pups killed by swift decapitation. For most slice culture experiments, pups were produced by cross-breeding C57BL/6J (RRID: IMSR_JAX:000664) with homozygous Thy1-YFP-H (RRID: IMSR_JAX:003782) mice, and the hemizygous YFP-expressing pups were used for preparing slices containing YFP-labeled neurons. We also used C57BL/6J wild-type pups that did not express any fluorescent proteins. In a subset of experiments, ZsGreen-labeled astrocytes were imaged in slices obtained from cross-breeding tamoxifen inducible heterozygous GFAP-cre mice (Tg(GFAP-cre/ERT2)1Fki (Hirrlinger et al., 2006)) and homozygous Ai6 (RRID: IMSR_JAX:007906) mice.

Rat line used for dissociated cell culture

Dissociated hippocampal neurons were prepared from embryonic day 18 Sprague-Dawley (RjHan:SD, Janvier Labs, Saint-Berthevin, France) rat fetuses, as described previously and outlined below (Kaech and Banker, 2006).

METHOD DETAILS

Organotypic slices of hippocampus

Organotypic slices were isolated from 5-7 day old mouse pups and cultured by the Gähwiler method (Gähwiler, 1988; Gähwiler et al., 1997; Tønnesen et al., 2011). Mouse pups were quickly decapitated and hippocampi were dissected out in cold GBSS (ThermoFisher Scientific) with 10 mM glucose (VWR) and 2 mM kynurenic acid (Sigma-Aldrich). Hippocampi were cut in 350 μm coronal slices using a tissue chopper (McIlwain), and individual slices were placed on 0.01% poly-L-lysine (Sigma-Aldrich) coated coverslips (12 mm x 24 mm; #1.5; CML). Slices were embedded for 30 min in 10 μL chicken plasma (Sigma-Aldrich) followed by 10 μl of 0.2% thrombin (VWR) in GBSS with 10 mM glucose, which coagulated to encapsulate the slice when mixed.

The coverslips with the slices were transferred individually to flat-bottomed culturing tubes (110 mm x 16 mm; Dutscher) with 750 μl medium containing 50% Eagle's basal medium (ThermoFisher Scientific), 25% HBSS, and 25% horse serum (ThermoFisher Scientific), supplemented with glutamine (ThermoFisher Scientific) and glucose. The tubes were sealed and placed in a roller drum at 10 rotations per hour at 35°C. Once a week 500 μL of medium was changed in the tubes. For experiments, a given coverslip with a slice was mounted in a perfused imaging chamber, and the slice was imaged from below through the glass coverslip, while it could be approached with electrophysiology electrodes from the top.

Primary hippocampal neuron culture

Primary rat hippocampal neurons were grown as Banker cultures in the proximity of supporting astroglia feeder cells (Kaech and Banker, 2006).

For harvesting primary neurons embryonic day 18 fetuses were dissected from pregnant Sprague-Dawley female rats after CO_2-inhalation anesthesia and swift decapitation, and hippocampi were isolated in HBSS without calcium, magnesium and bicarbonate (HBSS⁻), supplemented with 10 mM HEPES (ThermoFisher Scientific) and penicillin-streptomycin. After chopping with scissors, hippocampi were digested in HBSS⁻ with 10 mM HEPES and 0.25% trypsin, followed by trituration in HBSS⁻ with 10 mM HEPES. Primary neurons were plated on 18 mm poly-L-lysine coated glass coverslips at a density of 50,000 cells per coverslip. Three hours after plating, coverslips were flipped into 60-mm culturing dishes containing a previously established astroglia cell layer and grown in Neurobasal medium (ThermoFisher Scientific) supplemented with 2 mM L-glutamine (ThermoFisher Scientific) and 1 x NeuroCult SM1 Neuronal supplement (STEMCELL Technologies) at 37°C and 5% CO_2.

Astrocyte feeder layers were prepared from similar embryos 2-3 weeks prior, by triturating the cerebral hemispheres in HBSS⁻ with 10 mM HEPES, 0.5% trypsin and 0.1% DNase. Astrocytes were plated at 20,000 to 40,000 cells per 60-mm dish and cultured in MEM (Fisher Scientific) containing 4.5 g/l glucose, 2 mM L-glutamine and 10% horse serum until co-culturing with the primary neurons. All imaging experiments of primary neurons were performed at days 17-21 post plating.

3D-STED microscope

The custom-built STED microscopy setup was constructed around the body of an inverted microscope (Leica DMI6000 CS), as previously described (Tønnesen et al., 2011). The inverted microscope provided ideal imaging conditions by allowing imaging directly through the glass coverslip. We used either an oil objective (TIRF, HCX PL APO, 100X/1.47 NA, Leica), which is optimal for imaging within the first few micrometers of tissue beyond the glass interface, or a glycerol objective (HC PL APO 63X/1.30 NA, Leica) equipped with a correction collar to reduce spherical aberrations, extending depth penetration to tens of micrometers inside the tissue (Urban et al., 2011).

The excitation light was provided by a pulsed diode laser (λ = 485 nm, pulse width = 70 ps; PicoQuant, Berlin, Germany) triggered by TTL pulses from the STED laser source at 80 MHz. A variable delay was added to the TTL train to ensure that the synchronized STED and excitation pulses were optimally aligned in time. The STED beam was derived from Ti:Sa femtosecond laser source with a repetition rate of 80 MHz and emitting at 838 nm (MaiTai, Spectra-Physics), which was converted to λ = 597 nm by an optical parametric oscillator (OPO; APE, Berlin, Germany). The 597 nm wavelength of the STED beam corresponds to the far right emission spectrum of green/yellow fluorophores such as YFP and GFP, where it induces stimulated emission, but little direct excitation.

The STED pulses were broadened in time to ensure effective de-excitation and maximal resolution enhancement. The femtosecond STED pulses were pre-stretched to around 2 ps by passing the beam through a 25 cm glass rod (SF6), and then broadened further to around 70 ps by passing it through a 20 m long polarization maintaining single-mode fiber (Pure silica core, NA 0.12, Schäfter & Kirchhoff). The pre-stretching was done to protect the optical fiber from photo damage and to avoid non-linear effects in the fiber by high peak powers.

Spatial resolution enhancement in three dimensions was achieved by splitting the STED beam into two beams by means of a polarizing beam splitter and imposing separate phase delays on their wave fronts. One beam was shaped to enhance lateral resolution by creating a "doughnut" PSF, while the other beam enhanced axial resolution by a "bottle beam" PSF (Wildanger et al., 2009). The doughnut PSF was created by introducing a 2π delay vortex phase mask in the beam path (RPC Photonics, Rochester, NY, USA), while the bottle beam PSF was created by a 2 mm diameter annular π delay phase mask. The width of the bottle beam was adjusted by a telescope so that half of the beam (in terms of power) passed through the circular delay pattern to yield a symmetric PSF with zero intensity at its focus. By placing a rotatable λ/2-wave plate in front of the polarizing beam splitter that split the original beam, we could arbitrarily distribute the laser power between the doughnut and bottle beam. By recombining the doughnut and bottle beams using a second polarizing beam splitter, the compound PSF enhanced the spatial resolution in 3D.

The 3D-STED beam was precisely aligned with the excitation beam using a 590 nm short-pass dichroic mirror and a piezo-positioner. The overlaid beams passed through an x-y beam scanner (Yanus scan head, TILL Photonics), whose mirrors were conjugated to the back focal plane of the objective, and scanned across the sample. The fluorescence emission was collected episcopically, descanned, isolated from the incident beams using a 499 long-pass dichroic mirror, and cleaned up using a 525 ± 25 nm band-pass filter. The signal was focused into a multimode optical fiber (62.5 μm core diameter) connected to an avalanche photodiode (APD; SPCM-AQRH-14-FC; PerkinElmer), with the fiber acting as a confocal pinhole to reduce out-of-focus fluorescence.

The setup was designed for 3D-STED imaging of green and yellow fluorophores, such as YFP, GFP, calcein green, Alexa Fluor 488, Atto-488 and Atto-514.

A second Ti:Sa femtosecond laser beam was co-aligned with the STED and excitation beam using a 680 nm short-pass dichroic mirror and used to acquire 2-photon images (at λ = 935 nm) for comparison purposes, and to perform 2-photon glutamate uncaging at λ = 745 nm.

We performed two-color 3D-STED at tens of micrometers inside living brain tissue using the glycerol objective mentioned above. Two fluorophores with partially overlapping excitation and emission spectra (e.g., calcein green and YFP) were imaged simultaneously using a single common excitation/depletion laser beam pair, thereby facilitating spatial and temporal alignment of the two imaging channels and minimizing photon exposure. The sole difference to single color imaging was that the emission signal was split by a 514 nm long-pass dichroic mirror, and the two parts were sent into separate photo detectors (Tønnesen et al., 2011). The imaging depth and z stack stepping intervals were controlled via a piezo-driven objective nano-positioner for z axis scanning (PIFOC, Physik Instrumente).

The 2-photon laser intensity was controlled via a Pockels cell (350-80LA Electro-Optic Modulator, Conoptics) that was controlled either manually for adjusting imaging intensities or by voltage pulses (1 ms, variable amplitude) from the electrophysiology amplifier for glutamate uncaging. The STED beam intensity was controlled by a combination of a λ/2-plate and a polarizing beam splitter, while the excitation beam intensity was adjusted by an optical density filter mounted in a motorized linear translation stage.

Microscope performance was evaluated by measuring the PSFs of the laser beams, and by measuring the spatial resolution for a defined set of imaging parameters (5 mW STED power at the sample, 20 nm x 20 nm pixels, and 20 μs dwell time). PSFs were visualized by reflecting the individual laser beams on 150 nm gold nano-spheres, while spatial resolution was analyzed by imaging 40 nm fluorescent beads adhering to the surface of a glass coverslip. These beads served as point sources, and their apparent size is a

measure of the spatial resolution of the microscope. In addition to imaging beads on coverslip surfaces, gold and fluorescent beads were embedded in agar where the refractive index was adjusted to 1.36 by the addition of glycerol, matching roughly the refractive index of brain tissue. This helped us establish the optimal position of the correction collar of the glycerol immersion objective (Figure S1). The spatial resolution was around 175 nm (x-y) and 450 nm (z) for confocal imaging (λ = 485 nm) and around 260 nm (x-y) and 760 nm (z) for 2-photon imaging (λ = 935 nm). In diffraction-unlimited STED mode, the spatial resolution was around 60 nm (x-y) and 160 nm (z).

Extracellular labeling and imaging

For imaging, slices were transferred on their glass coverslip to a heated and perfused imaging chamber (32.5°C; 1-2 mL/min). The perfusion medium (artificial cerebrospinal fluid, ACSF) consisted of 125 mM NaCl, 2.5 mM KCl, 1.3 mM $MgCl_2$, 2 mM $CaCl_2$, 26 mM $NaHCO_3$, 1.25 mM NaH_2PO_4, 20 mM d-glucose, 7.5 mM HEPES, 1 mM Trolox, 1 mM ascorbic acid (all from Sigma-Aldrich); 300 mOsm; pH 7.4.

The extracellular dye, which was either Alexa Fluor 488 (0.57 kDa Hydrazide or 10 kDa dextran, ThermoFisher), calcein (Thermo-Fisher), Atto-514, or Atto-488 (both Atto Tec), was added from an ACSF-based 4 mM stock into the bulk ACSF while looping perfusion at a total volume of 20 to 30 mL, or pipetted directly into the chamber while pausing the perfusion. Both strategies worked equally well, with no discernible differences in slice viability for imaging sessions lasting tens of minutes to hours. The final fluorophore concentration was around 40 μM, corresponding to a 1:100 dilution of the stock. This could be adjusted on the fly by adding additional fluorophore or ACSF to the perfusion volume. For two-color imaging of ECS and fluorescently labeled cells, we kept the ECS fluorescence intensity around 50% lower than the intracellular label intensity, so that the two signals could be distinguished based on their relative intensity as well as spectral emission. Spectral detection of the two fluorophores worked well using a 514 nm dichroic mirror that split up the signal into two APDs. Direct injection of the dye into the tissue via patch pipettes provides an alternative ECS labeling strategy that is acute and local and uses up much less fluorophore than bath perfusion.

For live-cell imaging, we commonly operated with a doughnut-to-bottle beam power ratio of 1:2, and an overall STED power of around 25 mW measured at the objective back aperture. The beam intensities were adjusted on the fly, individually or for both beams simultaneously, depending on the sample and imaging depth. Pixel sizes were typically 20 nm x 20 nm in STED, and 40 nm x 40 nm in confocal and 2-photon mode, while pixel dwell times were between 10 to 20 μs.

When using the glycerol objective equipped with a correction collar we could obtain high-quality SUSHI images up to 50 μm below tissue surface. This depth agreed with the measurements of fluorescent beads embedded in agar described above, where spatial resolution was enhanced as deep as 70 μm in agar.

Electrophysiological whole-cell and field recordings

All electrophysiology experiments were obtained by means of a 700B MultiClamp amplifier and a Digidata 1440A digitizer (both from Axon Instruments/Molecular Devices) and using the glycerol objective. Whole-cell patch-clamp recordings of excitatory postsynaptic currents (EPSCs) were obtained from CA1 pyramidal neurons, through glass pipettes with a tip resistance of 3.5 to 4 MΩ. The intracellular solution contained 120 mM cesium-methanesulfonate, 5 mM CsCl, 1 mM EGTA, 4 mM Mg-ATP, 0.3 mM Na-GTP and 10 mM sodium phosphocreatine (all from Sigma-Aldrich), and 5 mM QX-314 (Tocris), adjusted to 290 mOsm/L and pH 7.3. The sampling rate was 10 kHz. To evaluate the effect of extracellular dye labeling on electrophysiological properties of the neurons, ACSF with 40 μM Alexa Fluor 488 was washed in for 10 to 30 min before patch-clamping a CA1 pyramidal neuron. After 10 min of voltage-clamp at −70 mV, we recorded 3 min of spontaneous EPSCs. Control experiments were performed in an identical fashion, in the absence of Alexa Fluor 488 in the ACSF. Input resistance was calculated from the steady state response to a test pulse (−5 mV, 10 ms).

Electrophysiological recordings of field potentials were obtained from the CA1 pyramidal cell layer in current-clamp mode using glass pipettes filled with ACSF and a tip resistance of around 2 MΩ. The sampling rate was 5 kHz. All electrophysiological recordings were performed at 32.5°C, as during the imaging experiments.

Analyzing ECS width and volume fraction

To measure the geometric width of structures, we obtained the full width at half maximum (FWHM) of Gaussian fits to 3-pixel wide line intensity profiles. The widths of unlabeled neural 'shadow' structures appeared as drops in fluorescence signal, and here the fitting was done to downward Gaussian curves.

As the added fluorophore rapidly distributed uniformly in the perfusion ACSF, variations in pixel intensities reflected physical displacement of the ACFS within a pixel area, rather than variations in fluorophore concentration. Pixel fluorescence intensity was therefore assumed to scale linearly with the ECS volume fraction in that pixel.

To estimate the ECS volume fraction in an image, we assigned to each pixel a value between zero and hundred percent ECS, corresponding to pure ECS, measured in larger identifiable ACSF-filled voids in the neuropil. We then binarized the image, so that pixels with intensities > 50% of the maximal value were considered ECS. The ECS volume fraction was defined as the number of above-threshold pixels divided by the total number of pixels ('binary' method; Figure 3 and Figure S6).

In an alternative approach, we estimated ECS volume fraction by calculating the average intensity of all pixels in a region of interest and dividing it by the maximal intensity value representing pure ECS ('integrative' method; Figure S6).

Hyper-osmolarity challenge

Osmolarity was raised in the perfusion ACSF from 300 mOsm/L to 370 mOsm/L by the addition of NaCl. After 10 minutes of hyper-osmotic perfusion, the perfusion solution was changed back the normo-osmotic ACSF. To make the hyperosmotic solution, NaCl was added to the normal perfusion ACSF from a high molarity stock solution, preserving the concentrations of the other ingredients of the ACSF, including the 40 μM calcein.

Epileptiform activity

To induce epileptiform discharges we blocked inhibitory GABA$_A$-receptor transmission by adding 50 μM picrotoxin (PTX, Ascent Scientific) to the fluorescent perfusion ACSF. During the experiment, we recorded time-lapse SUSHI images and concurrent electrophysiological field recordings, as described above.

Two-photon glutamate uncaging

Glutamate was uncaged from DNI-Glu-TFA (Femtonics), which was bath applied at 1 mg/mL in the perfusion ACSF. To reduce background neuronal activity, 2 μM TTX was added to the ACSF. The uncaging laser pulses were delivered at a wavelength of 745 nm at 1 ms duration and an intensity of 2.5 to 3.5 mW at the sample. The uncaging power was adjusted to produce consistent responses on dendritic spines of YFP-labeled CA1 neurons at the given imaging depth. Uncaging pulse duration, frequency and power were controlled by a Pockels cell via the electrophysiology amplifier and data acquisition software.

To induce structural changes in the ECS we delivered 30 uncaging pulses at 1 Hz, preceded and followed by time-lapse SUSHI at 0.7 frames/second. Control experiments were obtained with identical settings in the absence of the caged glutamate.

We analyzed the ECS intensity over the time-lapse frames in a 1 μm^2 area centered on the uncaging spot. For each frame, the average intensity inside the area of interest was calculated. We calculated the standard deviation (SD) of the signal for each pixel across the time lapse frames in the area of interest. We compared the average SD of the 1 μm^2 area around the uncaging spot to the SD of a control area of identical size within the same image frame (arbitrarily chosen at 2 μm to the right or left of the uncaging spot, avoiding any somas and large dendrites). The SD calculation of the time-lapse series was made using the 'Z-Project' function in ImageJ.

Two-photon laser lesions

Two-photon laser lesion experiments were performed to induce cell migration. Organotypic slices from wild-type mice were perfused in closed loop with 10 mL ACSF. For SUSHI imaging, calcein was added to the ACSF at a final concentration of 200 μM. To inflict small lesions, the 2-photon laser scanned a 1.5 μm x 1.5 μm area using a wavelength of 810 nm and 80 mW laser power measured at the back aperture of the objective. The field of view was 100 μm x 100 μm, pixel dwell time was 30 μs, and pixel size was 48.5 nm x 48.5 nm.

Image processing

Displayed images are single sections taken from z stacks or time-lapse series, as indicated. All morphometric measurements were done on raw images in ImageJ using the 'Plot Line Profile' function after drawing 3-pixel-wide straight lines through the area of interest. Gaussian fits were applied either directly in ImageJ, or after importing the line profiles into IGOR Pro. Fluorescence intensity within areas of interest was measured in ImageJ using the rectangular selection tool and the 'Measure' function. Displayed images were processed with a 1- or 2-pixel median filter in ImageJ to remove noise. No other image processing, such as deconvolution, was applied. Brightness and contrast were adjusted for each image using ImageJ's 'Brightness and Contrast' function.

Two-color images are shown as a merge of the filtered raw channels. The look-up tables (LUT) were *grays (inverted)* for ECS and *orange hot* for cellular structures. No spectral unmixing was done, as the fluorophore pairs were well distinguishable in the raw images.

3D reconstructions

Morphological 3D reconstructions were performed on SUSHI z stacks in ImageJ, by using the '3D Viewer' plugin. In each section of a given stack with an inverted LUT, a given non-fluorescent structure of interest was manually outlined and the surroundings cleared while the bit-depth was preserved. Using the '3D Viewer' plugin, individual structures were surface-rendered using a threshold at 10% of maximal pixel count, and each structure was saved separately as a raw TIFF file as well as a '3D Object' file. Finally, all surfaces from within the stack were merged as '3D Objects' into one volume and displayed in different colors.

QUANTIFICATION AND STATISTICAL ANALYSIS

Data were tested for normality using D'Agostino-Pearson omnibus test, and comparisons were made by appropriate parametric or non-parametric tests, taking into account number of groups and the nature of the data (paired/non-paired or repeated acquisition), as specified. Statistical tests were performed using Graphpad Prism. Normally distributed data are presented as mean with standard deviation, while non-normal data are presented as median with interquartile range. The significance level was set at 5%. The size and type of individual samples, n, for given experiments is indicated and specified in the results section and in figure legends. Asterisks in figures indicate p values as follows: * $p < 0.05$, ** $p < 0.01$, *** $p < 0.001$.
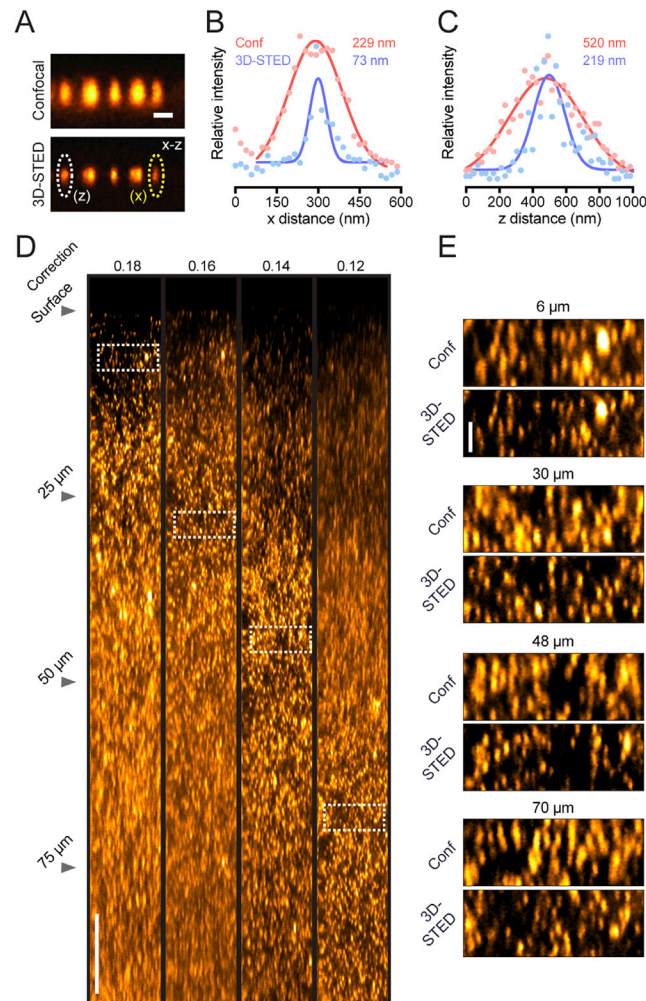
Supplemental Figures

Figure S1. Gain in Spatial Resolution by 3D-STED, Related to Figure 1

(A) Images of 40 nm fluorescent beads acquired by 3D-STED and confocal microscopy using a 1.3 NA glycerol immersion objective equipped with an aberration correction collar.

(B) Lateral (x) line profiles through the bead indicated in (A), imaged by confocal and 3D-STED. The indicated FWHM is a measure of the spatial resolution of the microscope.

(C) Axial (z) line profiles through the bead indicated in (A). FWHMs are indicated for the two lines.

(D) Consecutive 3D-STED x-z scans into the same sample of 40 nm fluorescent beads suspended in agar, the difference between the four images is the position of the correction collar, as indicated. The agar was adjusted with glycerol to have a refractive index of 1.36, corresponding to brain tissue. The surface corresponds to the glass coverslip interface. The effective focus is shifted as the objective correction collar is adjusted to the indicated values. The 0.12 correction setting represents the maximum correction and the most distant focus (around 70 μm). Scale bar is 10 μm.

(E) Zoom-ins of the areas in focus for a given correction collar setting, indicated by squares in (D). The 3D-STED images are shown next to a confocal image of the same area, confirming that 3D-STED resolution is preserved down to around 70 μm depth. Scale bar is 1 μm.
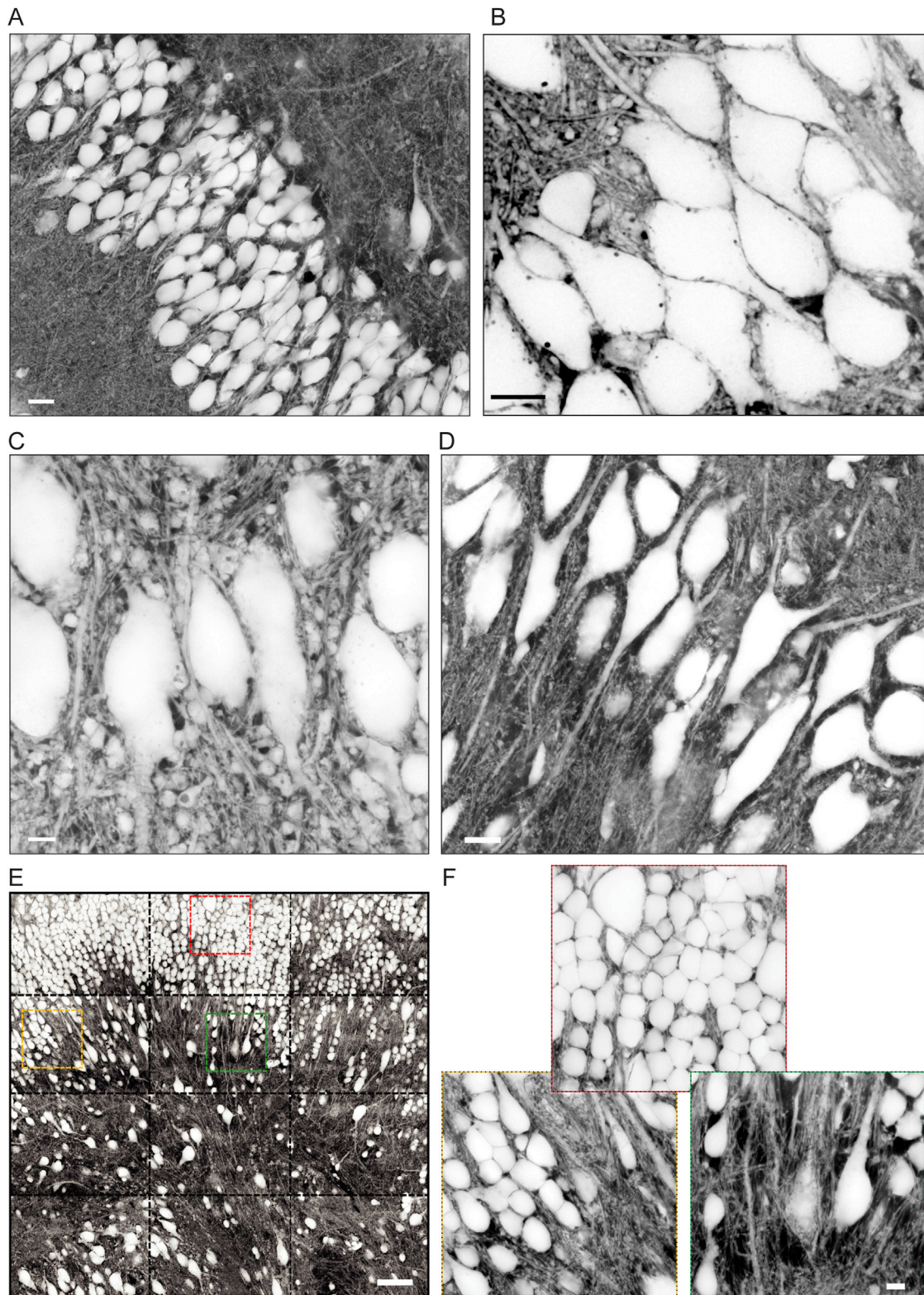
Figure S2. SUSHI of Living Hippocampal Slices, Related to Figure 1

(A) SUSHI image of the granule cell layer in hippocampus. Scale bar is 5 μm.

(B) SUSHI image of the CA1 pyramidal cell layer. Note black puncta/vesicles inside cell bodies, indicating uptake of dye by endocytosis. Scale bar is 5 μm.

(legend continued on next page)

(C) CA3 pyramidal cells with many large mossy fiber boutons visible in the surrounding neuropil. Scale bar is 5 μm.

(D) CA3 pyramidal cells. Scale bar is 10 μm.

(E) Mosaic image of twelve tiled frames of the dentate gyrus with granule cells at top. Scale bar is 50 μm.

(F) Color-coded zoom-ins on the areas outlined in (E), revealing large and variable patches of ECS. Scale bar is 5 μm.
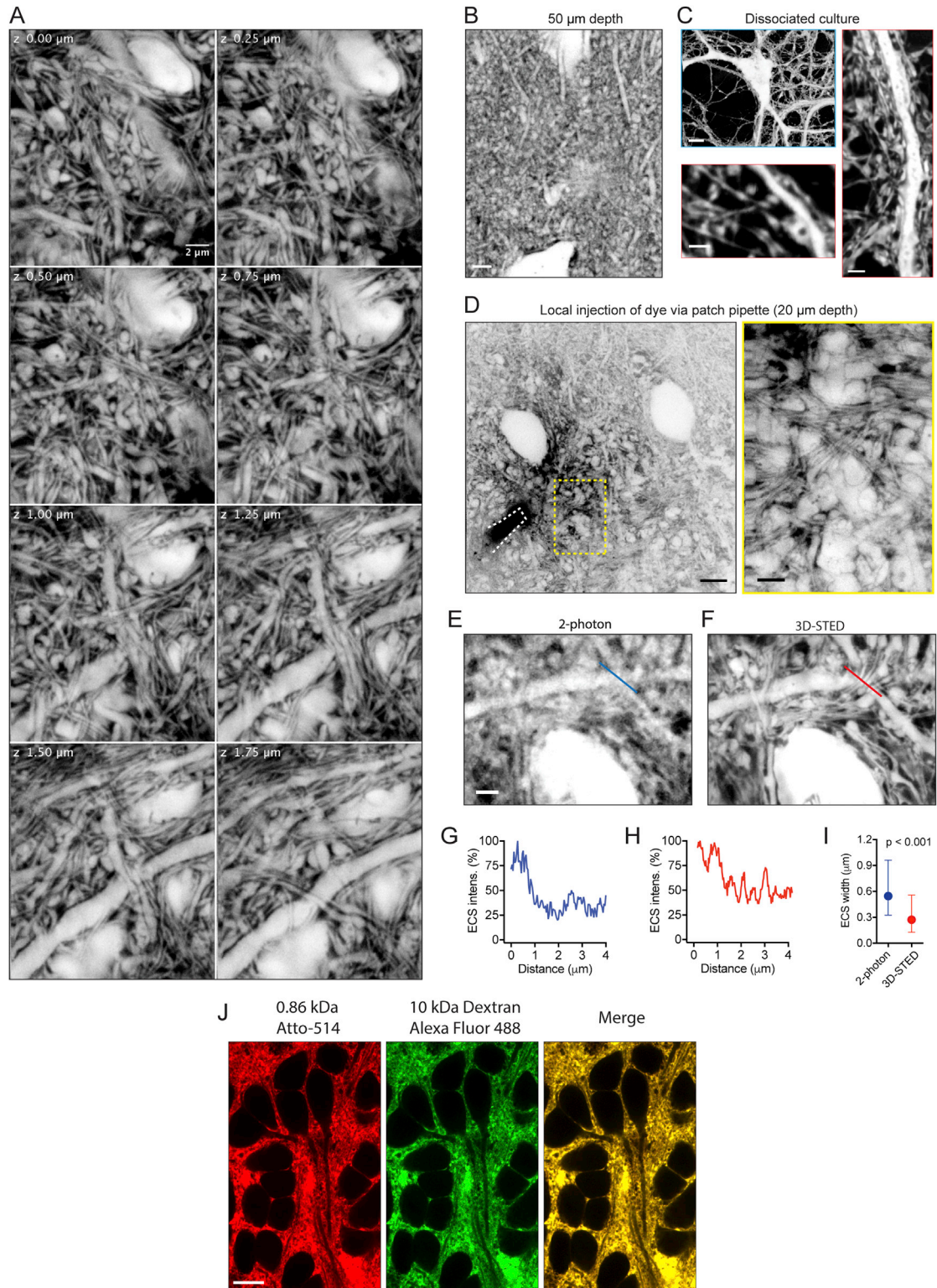
Figure S3. Versatility of Extracellular Labeling and Comparison to 2P-Microscopy, Related to Figure 1

(A) SUSHI z stack illustrating the complex 3D structure of brain tissue. Scale bar is 2 μm.

(B) SUSHI imaging at 50 μm tissue depth. Scale bar is 3 μm.

(C) Confocal inverted image of an unlabeled dissociated hippocampal neuron in culture (*blue frame,* scale bar 10 μm); and two examples of SUSHI of unlabeled dissociated hippocampal neurons, showing axonal boutons in contact with dendritic spines (*red frames,* left scale bar 4 μm, right scale bar 2 μm).

(D) Local injection of Alexa Fluor 488 into organotypic slice via patch pipette. The pipette tip is outlined by the dotted white line (Scale bar is 10 μm) with zoom-in on area outlined in yellow, though slightly shifted in z (Scale bar is 3 μm).

(E) 2-photon image of the ECS-labeled neuropil around a cell soma. Scale bar is 2 μm.

(F) The same frame imaged by 3D-STED.

(G) Intensity profile of the line shown in (A). Only large structures are discernible above the background as broad peaks in the plot, due to the limited spatial resolution that smoothens out higher spatial frequencies.

(H) The corresponding line intensity profile from the corresponding 3D-STED image (C) reveals several thinner peaks, reflecting thin putative axons that are not discernible by 2-photon microscopy.

(I) Comparison of ECS widths as measured by 2-photon and 3D-STED microscopy. Two-photon microscopy yields a significant larger median ECS width (n = 132 widths from 5 slices) and right-shifted range than 3D-STED (n = 620 widths from 9 slices), reflecting its lower spatial resolution (reported p value is from Mann-Whitney test). Graph shows median with interquartile range.

(J) Two-color SUSHI of ECS labeled with both Atto-514 (0.86 kDa) and dextran-Alexa Fluor 488 (10 kDa), and their merged image. The merge indicates that the two dyes penetrate equally well into the ECS, despite their size difference. Note that the images LUTs are not inverted. Scale bar is 10 μm.
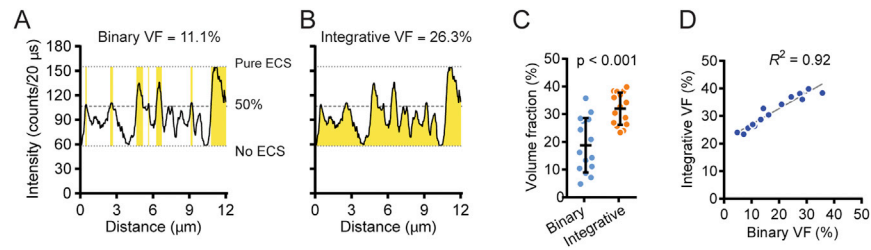
Figure S4. Measuring the Volume Fraction of Brain ECS, Related to Figure 3

(A) Calculation of the ECS volume fraction (VF), by binarization with a threshold of half the dynamic range of the pixel values (binary method, also depicted in Figure 3).

(B) Alternative calculation of the VF (integrative method). Line profile plot of intensity through the ECS. The minimum (background) and maximum (pure ECS) fluorescence values are measured and indicated by dotted lines. The value of each pixel represents its relative fraction of ECS, and the integrated pixel value across an image represents the overall ECS VF, here indicated as the yellow area relative to the total area between the min and max values.

(C) Pooled data for estimates of ECS volume fractions based on the binary and fractional methods, respectively (n = 15 areas from 10 slices). Each point is one area while bars depict mean with SD. The two approaches yield different results (paired t test, $p < 0.001$).

(D) While the two approaches yield different mean values, there is a near perfect correlation between them (linear regression, $R^2 = 0.92$).
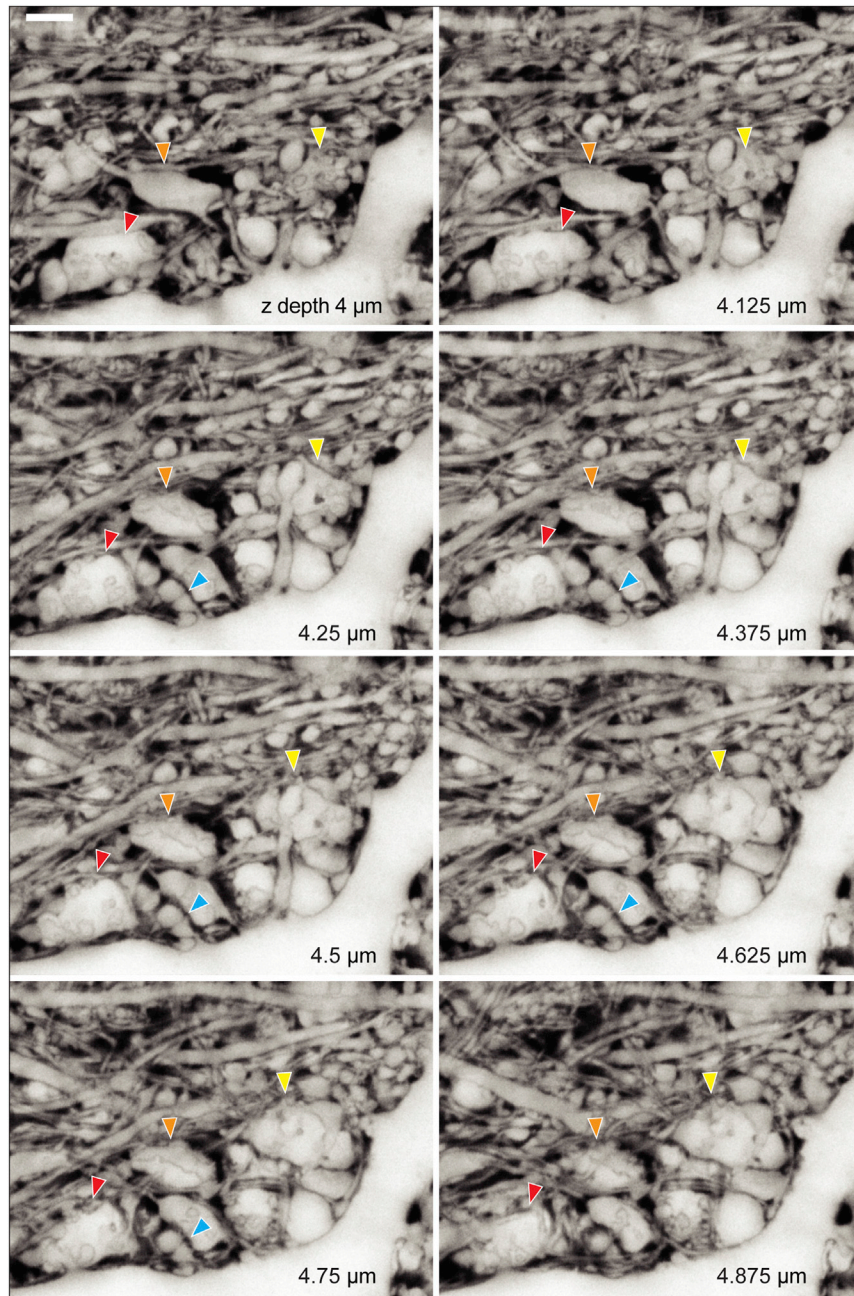
Figure S5. SUSHI Enables Detection of Putative Synaptic Clefts, Related to Figure 7

SUSHI z stack of the image section from Figures 7A and 7C, showing putative synaptic clefts formed between giant mossy fiber boutons and a thorny excrescences on a postsynaptic CA3 pyramidal neuron (yellow, orange and red arrows), and between a dendritic spine and a bouton (blue arrow). Scale bar is 3 μm.
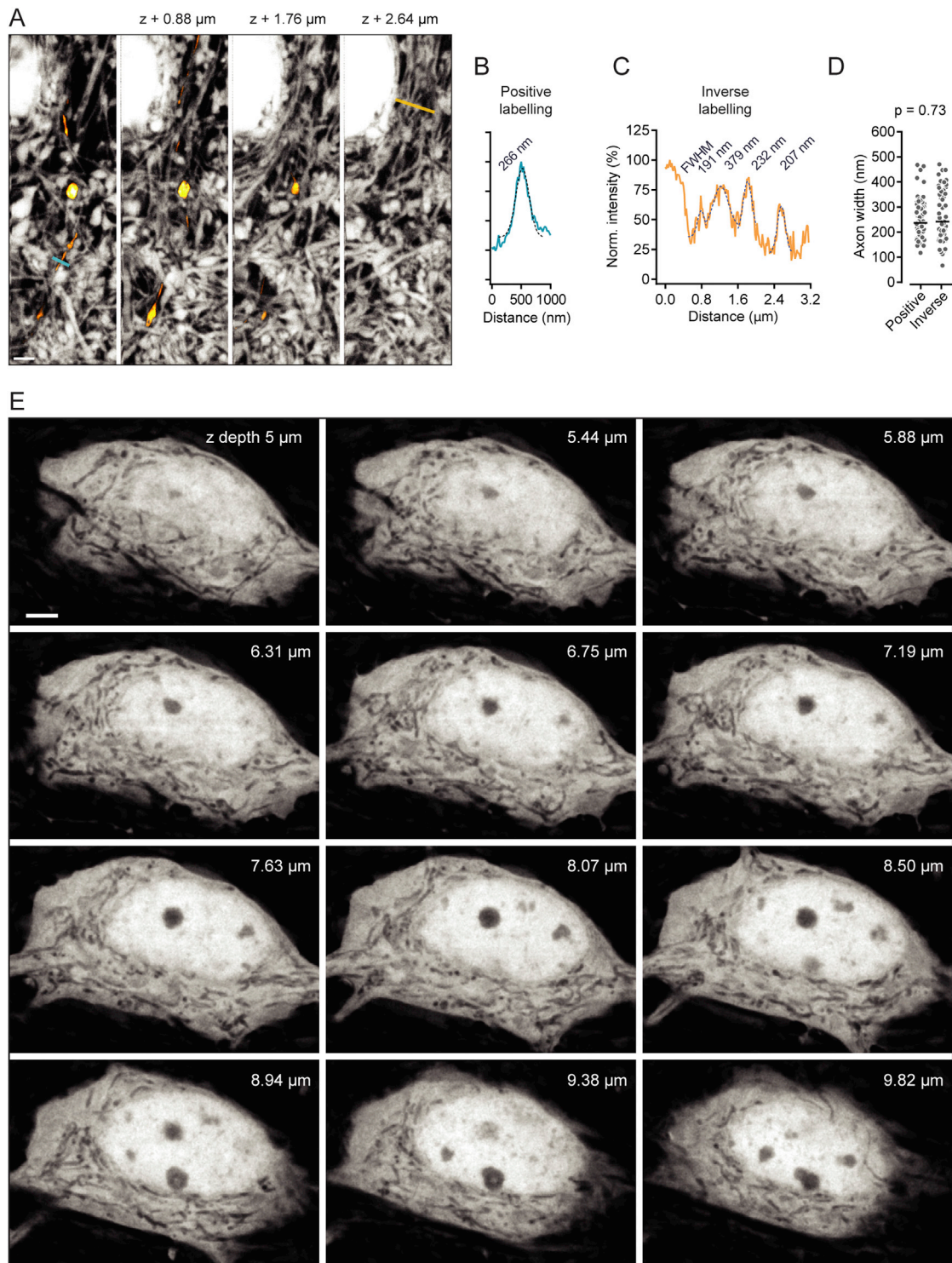
Figure S6. SUSHI Provides Access to Nanoscale Anatomical Information, Related to Figure 7

(A) Individual image sections from z stack of YFP-labeled axon and the surrounding neuropil imaged by two-color SUSHI and merged. Scale bar is 2 μm. The full SUSHI z stack is displayed in Movie S7.

(B) Intensity profile of the blue line through the YFP-labeled axon shown in the first section of (A). The line shows intensity in the YFP detection channel. A Gaussian fit is shown, along with the FWHM value.

(C) Intensity profile of the orange line through axons in the last section of (A). The peaks are fitted with Gaussian functions and the corresponding FWHMs are indicated.

(D) FWHMs of YFP-labeled axons and unlabeled axons imaged by SUSHI. Points represent individual FWHM measurements while bars indicate median (n = 66 positively labeled axons from 6 slices and 57 negatively labeled axons from 7 slices). The diameters between negatively and positively labeled axons did not differ (Mann-Whitney test, p = 0.73).

(E) Individual sections of a z stack of the raw YFP-channel through the soma of the YFP-labeled neuron shown in Figure 7. The nucleoli and organelles are clearly discernible as 'shadows' in the cytosol. Scale bar is 3 μm.
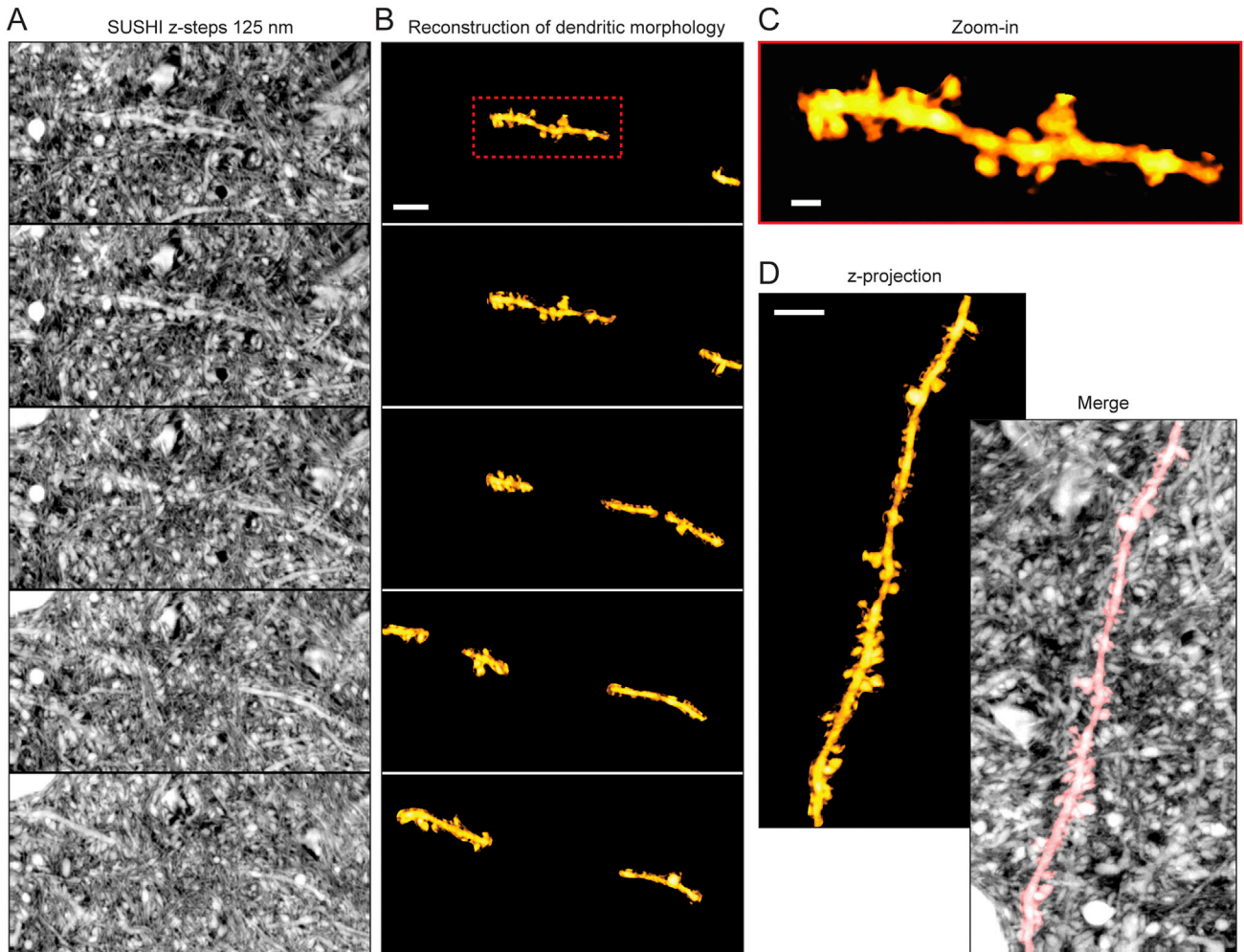
Figure S7. SUSHI for 3D Morphology Reconstructions of Unlabeled Live Cells, Related to Figure 7
(A) Individual image sections of z stack of neuropil imaged by SUSHI.
(B) The same stack as (A) illustrating an unlabeled dendritic segment traced through the individual sections. Scale bar is 4 μm.
(C) Zoom-in on the dendritic segment of the first section, corresponding to the red square in (B). Scale bar is 1 μm.
(D) Maximum-intensity projection of the tracked dendritic segment, and merge of the outlined dendrite (in red) with the z-projection of the original SUSHI stack, rotated right relative to A and B. Scale bar is 4 μm.